Mass spectrometric study of chemical reactions, molecular migrations, and interactions in dynamic organic systems

Inauguraldissertation

zur
Erlangung der Würde eines Doktors der Philosophie
vorgelegt der
Philosophisch-Naturwissenschaftlichen Fakultät
der Universität Basel
von

Maciej Kawecki

2020

Genehmigt von der Philosophisch-Naturwissenschaftlichen Fakultät
auf Antrag von:

Prof. Dr. Hans J. Hug
Prof. Dr. Ernst Meyer
Prof. Dr. Antonella Rossi

Basel, den 17. Dezember 2019

Prof. Dr. Martin Spiess, Dekan

Preface

This project was funded by the Swiss National Science Foundation (SNF) (grant number CR23I2-162828) and Empa, the Swiss Federal Laboratories for Materials Science and Technology. The project was carried out 2016-2019 at Empa Dübendorf, at the Laboratory for Nanoscale Materials Science, headed by Prof. Dr. Hans Josef Hug. The supervision of this thesis was shared between Dr. Rowena Crockett, Dr. Laetitia Bernard and Prof. Dr. Hans Josef Hug.

Time-of-flight secondary mass spectrometry (ToF-SIMS) measurements were carried out by Maciej Kawecki on the IONTOF.5 instrument stationed at Empa Dübendorf, at the Laboratory for Nanoscale Materials Science, headed by Prof. Dr. Hans Josef Hug. Light-emitting electrochemical cells (LECs) were prepared by Maciej Kawecki, Matthias Diethelm, Sandra Jenatsch and Quirin Grossmann at Empa Dübendorf, at the Laboratory of Functional Polymers, headed by Prof. Dr. Frank Nüesch. Quantum chemistry calculations were conducted by Dr. Daniele Passerone at Empa Dübendorf, at the Nanotech@Surfaces Laboratory, headed by Prof. Dr. Roman Fasel. The ToF-SIMS image of the uranium distribution across uranyl acetate-stained HeLa cells, used in Fig.1.1C as example for ToF-SIMS image generation, was acquired on a sample provided by Dr. Andres Käch, working at the Center for Microscopy and Image Analysis at the University of Zurich, in the course of a separate collaboration.

For a moment, nothing happened. Then, after a second or so, nothing continued to happen.

Douglas Adams (1952-2001), The Hitchhiker's Guide to the Galaxy

Abstract

Molecular interactions, recognition, and self-assembly are of central importance for the properties of organic materials and function of biological systems. Currently, there is no experimental method available that allows inter-molecular interactions to be probed at the scale of single molecules in non-crystalline organic matter. Often, molecular aggregation, self-assembly at single-nanometer scales, and nucleation processes remain beyond experimental reach. The presented work demonstrates that statistical molecular interaction probabilities, surroundings, and arrangement can be probed *in-situ* in organic matter by means of secondary ion mass spectrometry. Supramolecular assemblies containing 10 and more organic molecules linked by hydrogen bonds or dipole-π interactions are extracted under preservation of chemistry and structure. The compositional distributions of the assemblies extracted reveal molecular self-assembly at length-scales typically not accessible to electron microscopy or X-ray diffraction.

In dynamic organic systems, shifts in the spatial distributions of the different molecules can induce changes in the local chemical equilibria at nanometer length-scales. Work conducted in this thesis on thin-film organo-electronic devices with sub-100 nm layer thicknesses demonstrates that molecular distribution rearrangements and the resulting adjustments in chemical equilibira can be resolved in time by means of dual-beam depth profiling in secondary ion mass spectrometry and with sufficient depth resolution to resolve the interfacial formation of electric double-layers. The presented approach for the in-situ study of dynamical systems, while limited to thin-film electronics, provides insight into reversible field-induced molecular migrations and chemical processes where until now often only indirect information could be gained by means of e.g. capacitance measurements.

Zusammenfassung

Nonkovalente Wechselwirkungen zwischen organischen Molekülen, Molekülerkennung, und molekulare Selbstorganisation sind von zentraler Bedeutung für die Eigenschaften organischer Materie und die Funktion biologischer Systeme. Zur Zeit existiert keine Messmethode, welche es erlauben würde, die Wechselwirkungen zwischen Molekülen in nicht-kristalliner organischer Materie auf einer Molekül-zu-Molekül-Basis zu studieren. Oft bleiben molekulare Aggregation, Selbstorganisation auf Nanometerlängenskalen und Nukleationsprozesse jenseits des experimentell Erreichbaren. Die vorliegende Arbeit zeigt auf, dass statistische molekulare Umgebungen, Wechselwirkungswahrscheinlichkeiten, und Anordnung in complexer organischer Materie mit Hilfe von Sekundärionenmassenspektrometrie untersucht werden können. Hierbei werden supramolekulare Ansamlungen, welche aus 10 und mehr organischen Molekülen bestehen, die durch Wasserstoffbrücken oder Dipol-π Wechselwirkungen zusammengehalten werden, unter Beibehaltung lokaler Chemie und Anordnung aus organischer Materie gelöst. Die Verteilung der molekularen Zusammensetzungen der herausgelösten Ansamlungen offenbart molekulare Selbstorganisation auf Längenskalen welche für gewöhnlich weder von Elektronenmikroskopie noch Röntgendiffraktometrie aufgelöst werden können.

In dynamischen organischen Systemen können Änderungen der Räumlichen molekularen Verteilungen zu Verschiebungen localer chemischer Gleichgewichte auf Nanometerlängenscalen führen. Hier durchgeführte Arbeit an Dünnschichtelektronik zeigt auf, dass molekulare Migrationen und daraus resultierende Änderungen chemischer Gleichgewichte *in-situ* mit Hilfe von sekundärionenmassenspektrometrischer Tiefenprofilierung zeit-aufgelöst werden können, und dies in eiener Tiefenauflösung welche es erlaubt die Formation elektrischer Doppelschichten an Grenzflächen zu untersuchen. Der vorgeführte Ansatz für die *in-situ* Untersuchung dy-

namischer Systeme beschränkt sich auf Dünnschichtelektronik, erlaubt jedoch das Studieren reversibler, feld-induzierter, molekularer Migrationen und chemischer Prozesse wo zuvor oft nur indirekte Informationen erhalten werden konnten, z.B. mit Hilfe von Kapazitätsmessungen.

Contents

Comprehensive list of content published over the study duration

[1] M. Kawecki*, R.Hany, M.Diethelm, S.Jenatsch, Q.Grossmann, L.Bernard* and H.J. Hug; *Direct measurement of ion redistribution and resulting modification of chemical equilibria in polymer thin film light-emitting electrochemical cells*; ACS Appl. Mater. Interf. **10**, 39100 (2018)

[2] S. Bai*, P. Da, C. Li, Z. Wang, Z. Yuan, F. Fu, M. Kawecki, X. Liu, N. Sakai, J.T.-W. Wang, S. Huettner, S. Buecheler, M. Fahlman, F. Gao* and H.J. Snaith*; *Planar perovskite solar cells with long-term stability using ionic liquid additives*; Nature **571**, 245-250 (2019)

[3] W. Xu, Q. Hu, S. Bai, C. Bao, Y. Miao, Z. Yuan, T. Borzda, A.J. Barker, E. Tyukalova, Z. Hu, M. Kawecki, H. Wang, Z. Yan, X. Liu, X. Shi, K. Uvdal, M. Fahlman, W. Zhang, M. Duchamp, J.-M. Liu, A. Petrozza, J. Wang, L.-M. Liu*, W. Huang* and F. Gao*; *Rational molecular passivation for high-performance perovskite light-emitting diodes*; Nature Photonics **13**, 418-424 (2019)

[4] F. Fu*, S. Pisoni, Q. Jeangros, J. Sastre-Pellicer, M. Kawecki, A. Paracchino, T. Moser, J. Werner, C. Andres, L. Duchene, P. Fiala, M. Rawlence, S. Nicolay, C. Ballif, A. N. Tiwari and S. Buecheler; *I2 vapor-induced degradation of formamidinium lead iodide based perovskite solar cells under heat-light soaking conditions*; Energy & Environmental Science **12**, 3074-3088 (2019)

[5] M. Diethelm, Q. Grossmann, A. Schiller, E. Knapp, S. Jenatsch, M. Kawecki, F. Nuesch and R. Hany*; *Optimized electrolyte loading and active film thickness for*

sandwich polymer light-emitting electrochemical cells; Adv. Opt. Mater., 1801278 (2019)

[6] M. Diethelm, A. Schiller, M. Kawecki, A. Devizis, B. Blülle, S. Jenatsch, E. Knapp, Q. Grossmann, B. Ruhstaller, F. Nüesch and R. Hany*; *The dynamic emission zone in sandwich polymer light-emitting electrochemical cells*; Adv. Funct. Mater., 1906803 (2019)

[7] M. J. I. Airaghi Leccardi, N. A. L. Chenais, L. Ferlauto, M. Kawecki, E. G. Zolliger, and D. Ghezzi*. *Tailored polymeric, photovoltaic, and near-infraredresponsive neuroprosthesis.* Nature Communications, in review

[8] M. Kawecki* and L. Bernard; *Database of proteinogenic amino acid reference spectra for bismuth-cluster ToF-SIMS. I. Negative polarity*; Surf. Sci. Spectra **25**, 015001 (2018)

[9] M. Kawecki* and L. Bernard; *Database of proteinogenic amino acid reference spectra for bismuth-cluster ToF-SIMS. II. Positive polarity*; Surf. Sci. Spectra **25**, 015002 (2018)

[10] L. Bernard, R. Crockett and M. Kawecki*, *Monosaccharides: a ToF-SIMS reference spectra database. I. Negative polarity*; Surf. Sci. Spectra **26**, 025001 (2019)

[11] L. Bernard, R. Crockett and M. Kawecki*, *Monosaccharides: a ToF-SIMS reference spectra database. II. Positive polarity*; Surf. Sci. Spectra **26**, 025002 (2019)

[12] M. Kawecki*, L. Bernard, D.Passerone, H.J. Hug and R. Crockett; *Supramolecular secondary ions reveal molecular interactions in organic matter*; submitted

[13] A. Mairena M. Baljozovic, M. Kawecki, K. Grenader, M. Wienke, K. Martin, L. Bernard, N. Avarvari, A. Terfort, K.-H. Ernst* and C. Wäckerlin*; *The fate of bromine after temperature-induced dehydrogenation of on-surface synthe-*

sized bisheptahelicene; Chemical Science **10**, 2998 (2019)

[14] T. Razafiarison C.N. Holenstein, T. Stauber, M. Jovic, E. Vertudes, M. Loparic, M. Kawecki, L. Bernard, U. Silvan and J.G. Snedeker*; *Biomaterial surface energy-driven ligand assembly strongly regulates stem cell mechanosensitivity and fate on very soft substrates*; PNAS **115**, 4631 (2018)

[15] M. Kawecki*, *Bitcoin mining built on shifting sands*; Nature **557**, 166 (2018)

* corresponding author

1 Introduction

In a broad sense, the goal of this thesis is to expand the application of mass spectrometry in studies of organic and biological matter using the ability to probe molecular migrations and inter-molecular interactions in dynamic systems. The first half of the thesis centers on thin film electronic devices containing organic molecules. The in-situ study of chemical processes and molecular migrations in operating organic electronic thin film devices is demonstrated and discussed. In the second half of this thesis it is shown that supramolecular constructs can be routinely extracted undamaged as secondary ions from complex organic matter. The extraction and mass spectrometric analysis of clusters consisting of weakly bound molecules allows the probing of molecular interaction probabilities and the revelation of hitherto invisible supramolecular arrangements in chemically rich molecular systems.

1.1 Secondary ion mass spectrometry

Detailed information on the principles underlying time-of-flight secondary ion mass spectrometry is provided, for example, in the book ToF-SIMS: Materials Analysis by Mass Spectrometry, Eds. J.C. Vickermann & D. Briggs.[1] *The following section aims to briefly summarize the science behind secondary ion mass spectrometry in general and ToF-SIMS in particular.*

The physics behind time-of-flight secondary ion mass spectrometry
Mass spectrometric techniques allow the chemical compositions of gasses, fluids and solids to be probed by ionizing part of their content and subsequently determining the mass-to-charge ratios of the generated ions. Whether a mass spectro-

metric technique is effective in analyzing gasses, fluids or solids is defined by the ionization mechanism used. It is also the ionization mechanism together with the target studied that define whether the set of generated ions predominantly consists of elemental ions, fragments, molecular ions or molecular assemblies. Ionization mechanisms inducing low molecular fragmentation are termed soft, and ionization mechanisms inducing strong molecular fragmentation, which are also unable to preserve most non-covalent interactions, are termed hard. A given mass spectrometric technique can be further subdivided into categories by how the mass-to-charge ratios of the generated ions are determined. The instrumentation determining the ion mass-to-charge ratio is called the analyzer, and the analyzer choice defines the specialization of a given instrument, allowing e.g. for particularly high mass resolution or sensitivity.

Secondary ion mass spectrometry (SIMS) is a technique designed to probe the elemental and molecular composition of solid matter. In SIMS, a well defined beam of charged atoms or atomic clusters is directed towards a surface. The ions of this beam are termed primary ions. Upon impact of a primary ion, molecules, molecular fragments and atoms are ejected from the surface or desorb from it as result of the energy dissipated from the primary ion (Fig. 1.1a). Only a fraction of the ejected or desorbed species possess an electric charge (typically, $< 1\,\%$). It is only this fraction that can be detected by the analyzer. Ions originating from the surface are termed secondary ions. Hence the name secondary ion mass spectrometry. An atom or molecule desorbed from the surface and possessing an electric charge is accelerated using an electric field. Each secondary ion of equal electric charge and accelerated along the same path by the same electric field gains the same kinetic energy, $E_{kin} = 1/2mv^2$. Secondary ions with different mass-to-charge ratios will have different velocities after passing through the field. The accelerated secondary ions fly through a field-free region and the time it takes for each ion to travel a well defined distance is measured. For each ion, the time of flight is strictly related to its mass-to-charge ratio and the ions with the lowest mass-to-charge ratio travel the distance in the shortest time. Unsurprisingly, the setup that uses this principle to determine the mass-to-charge ratio of an ion is called a time-of-flight (ToF) analyzer[2]. ToF analyzers typically reach mass resolving powers of

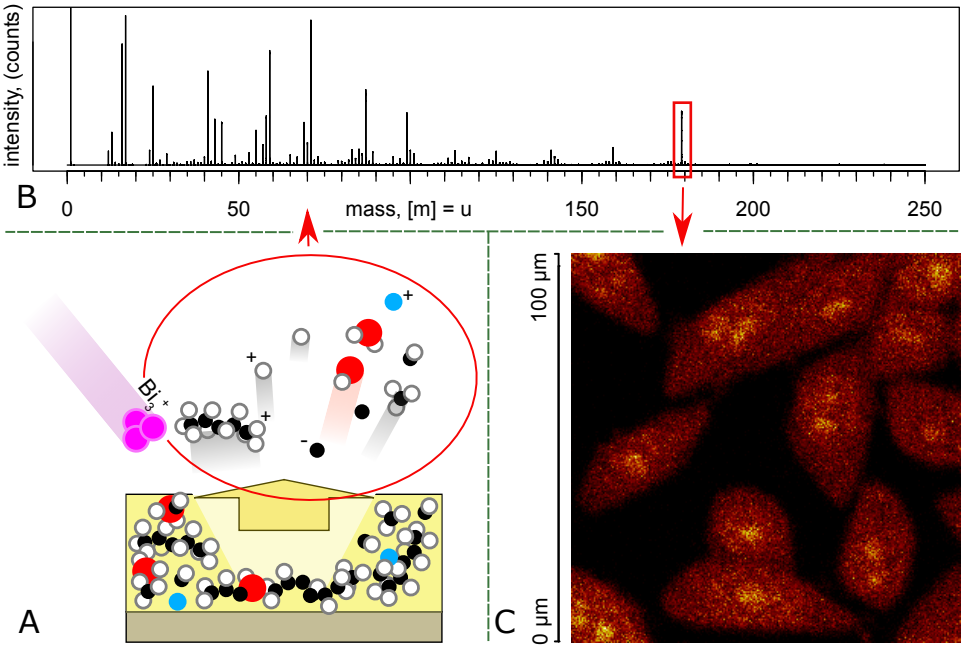

Figure 1.1: **Time-of-flight secondary ion mass spectrometry (ToF-SIMS). a)** Ionization process in SIMS: A primary ion, here a Bi_3^+ atomic cluster, impacts the surface to be analyzed. The impact ejects molecules, molecular fragments and atoms. Part of the ejected species is ionized. **b)** ToF-SIMS mass spectrum: Secondary ions of either positive or negative charge are separated by mass in the time-of-flight analyzer. **c)** ToF-SIMS imaging: a mass spectrum can be acquired on surfaces as small to $100 \times 100\ nm^2$, allowing the distribution of each secondary ion across the sample surface to be tracked. The image in panel c) was acquired on a cross-section of HeLa cancer cells.

5'000-10'000 m/Δm and their strength lies in the ability to record a continuous spectrum (see Fig. 1.1b) containing the entire mass range of secondary ions (up to a set cut-off), as opposed to detecting only ions with set mass-to-charge ratios (see e.g. the orbitrap analyzer[3]).

In SIMS, if the primary ion beam used to probe the surface is focused and scanned across the surface, images are generated with each pixel containing a mass spectrum and the pixel size being limited by the beam spot diameter (typically 100-300 nm). Correspondingly, for each time-of-flight interval, the origin of the secondary ions contained in this interval can be traced (see Fig. 1.1c). In addition to scanning with the primary ion beam, the surface can be removed layer-by-layer through sputter ablation using an additional sputter gun. This sputter gun allows chemical distributions as a function of depth to be investigated (typically a depth resolution of 2-5 nm can be obtained[4,5], but the depth resolution depends strongly on the material). Correspondingly, in the best case SIMS can map the chemical composition of a solid in three dimensions with a lateral resolution down to 100 nm and a depth resolution typically below 10 nm. Some of the limitations of SIMS encountered, however, in praxis, shall become apparent in the following sections.

The chemical principles relevant for molecular fragmentation and secondary ion formation

Only those chemical species ejected by primary ion impact that acquire an electric charge are visible to the mass spectrometer. Further, because only a fraction of the ejected molecules, molecular fragments and atoms acquires an electric charge, the abundance of a given secondary ion does not only depend on the abundance of its precursor on the surface area impacted, but also the ionization potential of the species in question. In the case of unfragmented molecular ions, the acquisition of an electric charge can, for example, occur through acceptance or loss of an electron or through the acceptance or loss of a proton (H^+). Correspondingly, in order for the unfragmented molecule to occur among the secondary ions, the molecule in question should be able to donate or accept a proton or electron. However, this requires the presence of a nearby molecule to accept the donated proton/electron

or donate the accepted proton/electron. Thus, the ionization probability defining the abundance of a given secondary ion is also a function of the statistical chemical neighborhood of the molecule in question on the probed surface. Further, as increasing the concentration of a given molecule on the surface inadvertedly alters the molecules statistical neighborhood, its detection rate may not scale linearly and in extreme cases can even decrease/increase with increasing/decreasing concentration of the molecule (well visible in [[6]] Fig. 5, top panel). The ensemble of mechanisms governing the interplay between detection rates and chemical neighborhoods are often grouped under the term matrix effects[7]. Due to the prevalence of matrix effects, SIMS results are in the simple case non-quantitative without consideration of additional input. SIMS is commonly classified as a hard ionization technique and the detected secondary ions are largely molecular fragments as opposed to unfragmented molecular ions. The fragmentation pattern of any given molecule provides a finger-print like signature. Single characteristic fragments are commonly used as proxy for the unfragmented molecules, and sets of fragment secondary ions may allow structural isomers to be distinguished[8]. The statistical composition of the generated molecular fragments depends largely on the individual bond strengths within the precursor molecules, however, the statistical composition of the subset of fragment secondary ions depends on the molecular orbitals of the precursor molecules and on charge transfer pathways. SIMS techniques are divided into static and dynamic SIMS. In static SIMS, such as ToF-SIMS, the accumulated ion dose density throughout a single measurement is kept low enough to statistically avoid a primary ion impact at a position already affected by prior impact damage. The dose density threshold following which the detected secondary ions undergo a gradual change due to cumulative ion impact damage is commonly termed the static limit. A common rule of thumb to ensure measurements below the static limit is to maintain an accumulated primary ion dose density below 10^{12} ions/cm^2 throughout a single measurement. However, ion impact damage may be observed even at lower dose densities and the onset is material-dependent. Measurements where a sputter beam is used in addition to the primary ion beam, that is dual beam depth profiling measurements and most 3D-imaging, by definition exceed the static limit. In order to minimize ion impact-induced changes to the local chemistry, the sputter ion beam typically has a far lower energy than the

primary ion beam but an ion current that is 5-6 orders of magnitude higher. The combination of low ion energy and high fluence minimizes potential fragmentation induced by sputter ion impact and results in a sputter crater with low surface roughness. It should be noted that the surface charging due to implanted sputter ions can induce migrations of easily ionizable species in the bulk[9,10].

The secondary ion mass spectrometric analysis of organic and biological samples

For a long time, the application of SIMS was limited to probing the spatial distribution of specific elements, as is of importance for example in the semiconductor industry. The path towards systematic studies of chemically rich organic and biological material was paved by the commercialization of atomic cluster primary ion beams such as the now standard bismuth liquid metal ion gun[11,12]. Primary ions consisting of atomic clusters allow the energy transferred upon impact to be distributed over a larger area, which results in significantly lower fragmentation of organic molecules present on the target surface. While molecular SIMS was discussed already in the 1980's[13], it is this transition towards atomic cluster ion sources that allowed systematic large scale studies of biological specimen by means of SIMS.

Modern instruments have a sub-100 nm lateral resolution[14], allowing the chemical imaging of single cell cross-sections. Independently, mathematical data processing tools such as principal component analysis[15] (PCA) have been implemented, allowing composition changes to be tracked across surfaces/cross-sections studied by imaging even at low secondary ion yeilds[16,17], or between mass spectra acquired on highly similar complex organic samples[18]. Further, dedicated sample environments and adapted instruments allow biological samples maintained at liquid nitrogen temperature to be probed.

For depth profiling, gas cluster ion beams[19] (GCIBs) were developed allowing the sputter-induced ion impact damage to be strongly reduced[20]. This was achieved using singly charged clusters of over 1000 atoms for the layer-by-layer sputter ab-

lation. GCIB sputter guns are currently employed in the study of organic thin film electronics.

Recent research efforts are directed towards the post-photoionization of the molecules and molecular fragments that are desorbed as a result of the primary ion impact but which do not possess a charge. The diverse approaches are grouped under the term secondary neutral mass spectrometry[21] (SNMS). A measurement technique relying on post-ionization of secondary neutrals can be expected to both increase detection rates and decouple the latter from chemical neighborhood-dependent ionization potentials.

1.2 Open challenges in mass spectrometry of organic and biological materials systems

Detection and resolution limits. SIMS is a destructive measurement technique. The molecules fragmented and/or ejected from a surface upon primary ion impact are lost to future analysis. Simultaneously, there is only a finite number of molecules in a given area or in a given volumetric cube of the target sample. Correspondingly, the lateral resolution and detection limits are strictly related. While studies show that measurements with resolutions down to ca. 15 nm can be theoretically conducted[14], in praxis such resolutions can only be attained in rare exceptions, due to insufficient signal-to-noise ratios. The limited number of molecules in a given voxel, together with the further limiting ionization and fragmentation probabilities provide a natural barrier to the spatial resolution attainable by SIMS. The main bottleneck is currently the ionization efficiency of below 1 % without dedicated post-ionization measures (see SNMS[21]).

Dynamic processes. SIMS at its most basic is not designed for time-resolved studies.

Non-covalent interactions. SIMS is considered a hard ionization technique,

and the current consensus is that only strong interactions such as through covalent bonds or in organo-metallic complexes can be preserved.

3D-imaging in biology. SIMS is a surface-sensitive technique able to chemically map a surface of several millimeters in diameter. However, 3D images generated in combination with dual-beam depth-profiling are limited in depth to a layer of approximately 1 µm due to accumulative surface roughness and chemical intermixing with increasing depth. This is sufficient for the study of thin film structures, but not for most biological structures which would require true 3-dimensional imaging. Note, already a single eucariotic cell typically extends over multiple micrometers in all three dimensions.

1.3 Mass spectrometric assessment of chemical processes and supramolecular interactions in dynamic organic and biological materials systems

This doctoral study approached, to varying degrees, the last three points listed: dynamic processes, non-covalent interactions, and 3D-imaging. The written thesis centers on dynamic processes and non-covalent interactions. Firstly, it is shown that certain dynamic processes can be routinely studied in-situ by developing an approach that reveals molecular migrations and chemical reactions within operating thin film organic and organic-inorganic electrical devices (sections 2.3 and 2.4). Secondly, it is shown that weak molecular interactions such as hydrogen bonds and dipole-π interactions can be routinely preserved during secondary ion formation, thus revealing hitherto hidden supramolecular interactions, structures and networks in complex organic matter (chapter 3).

Additionally to the work presented in the written thesis, first steps have been taken towards the development of a block-face imaging approach akin to the one

known from electron microscopy[22], aiming to generate 3D-images by means of an in-situ microtome mechanically sectioning the sample inside the instrument. The two microtome prototypes designed and assembled are not discussed in this written thesis and will be the center of future work. Sample preparation protocols for the ToF-SIMS block-face imaging of biological specimen are summarized in section SI4.

In addition to the research work conducted, databases of reference spectra were assembled for all proteinogenic amino acids + glycnie, and the monosaccharides allose, arabinose, fructose, fucose, galactose, 2-deoxygalactose, galacturonic acid, glucose, glucuronic acid, mannose, myoinositol, rhamnose, ribose, 2-deoxyribose, xylose, N-acetylgalactosamine, N-acetylglucosamine, N-acetylmuramic acid, and N-acetylneuraminic acid. These databases were published as the following series of four publications, the content of which is not repeated in the thesis:

[1] M. Kawecki and L. Bernard; *Database of proteinogenic amino acid reference spectra for Bismuth-cluster ToF-SIMS. I. Negative polarity*; Surf.Sci.Spectra **25**(1), 2018

[2] M. Kawecki and L. Bernard; *Database of proteinogenic amino acid reference spectra for Bismuth-cluster ToF-SIMS. II. Positive polarity*; Surf.Sci.Spectra **25**(1), 2018

[3] L. Bernard, R. Crockett and M. Kawecki, *Monosaccharides: a ToF-SIMS reference spectra database - Part 1/2: negative polarity*; Surf.Sci.Spectra **26**(2), 2019

[4] L. Bernard, R. Crockett and M. Kawecki, *Monosaccharides: a ToF-SIMS reference spectra database - Part 2/2: positive polarity*; Surf.Sci.Spectra **26**(2), 2019

2 ToF-SIMS study of thin-film electronic devices containing organic molecules

2.1 Introduction - Mass spectrometric tracking of dynamic processes

SIMS is by nature a destructive technique. Cumulative ion impact damage and implantation are an obstacle to time-dependent in-situ probing of dynamic processes by means of SIMS. Surface reactions can be studied by sufficiently lowering the primary ion current to remain below the static limit during the entire duration of the chemical process one aims to track. The author of this thesis is aware of one single attempt to study the progression of a surface reaction over time by means of SIMS: an unpublished demonstration of the temperature dependence of catalytic ammonia formation on a catalytic surface conducted by Dr. Laetitia Bernard (Empa, Switzerland).

Reducing the primary ion fluence allows in-situ surface reactions to be studied, but bulk processes such as molecular spatial redistributions cannot be studied by this approach. The destructiveness of dual beam depth profiling allows only one specific moment in time to be captured per measurement location and requires the relevant process to be halted for the measurement duration e.g. by lowering the sample temperature. Provided that a series of samples can be fabricated reproducibly or a series of identical samples can be retrieved, e.g. from a biological system or process, the limitation posed by the destructiveness of the measurement

approach can be overcome by studying the same process across multiple samples, each sample analyzed at a different point in time with respect to the onset of the process studied. In this thesis, it is demonstrated that this approach allows ionic migrations, degradation processes, and reversible changes in chemical equilibria across operating thin film electronic devices to be tracked in-situ (sections 2.3 and 2.4).

2.2 Introduction - Organic and organic-inorganic thin film electronics

Thin film electronic devices typically have a planar geometry and consist of a stack of different thin layers that each range in thickness from 1 nm to 1 µm. Applications of thin film electronics containing organic molecules span light-emitting devices such as organic light emitting diodes (OLEDs)[23], solar cells[24,25], sensory devices[26], and capacitors[27].

The research and development of thin film electronic devices commonly relies on scanning electron microscopy (SEM) for the visualization of degradation-induced changes in film cross-section morphology ([28], Fig. 3) or SEM energy dispersive spectroscopy by X-rays (EDX) to probe the elemental distribution across the film ([28], Fig. 4). Among the many analytical techniques used to gain supplementary information, SIMS dual-beam depth profiling allows molecular distributions across thin films to be probed.

In the development stage of a device, SIMS is typically used to, firstly, gain understanding of the layer compositions and vertical homogeneity, and, secondly, unravel chemical degradation pathways by analysis of failed devices. At the later stage of process engineering, information on molecular distributions as provided by SIMS can allow to rationally fine-tune device fabrication conditions. It is not uncommon, that differences in the deposition processes for single layers of a thin film organic-electronic device have a major influence on the performance of the device as a whole. This is because the process by which single layers are deposited

can influence both the degree of chemical intermixing at interfaces and, in organic films consisting of two and more molecular species, the nano-scale phase morphology of the bulk[29].

The thin film electronic devices studied in this thesis include light-emitting devices[10,30,31,32], solar cells[33,28], and retinal implants[34]. The development of a methodology for the study of ionic migrations and chemical processes that occur across operating thin film electronic devices was of particular interest. For this, a light-emitting device called the light-emitting electrochemical cell (LEC) was used as model system. LECs consists of a single thin film sandwiched between two electrodes, and the function of an LEC relies on a reversible spatial re-distribution of ions contained within this film before the onset of light-emission. The correlation between the light-emission of an LEC and the distribution of mobile ions within the device makes LECs particularly convenient model systems for the exploration of new experimental techniques to study dynamic processes in operating electronic devices. The emitted light of an LEC operated inside the ToF-SIMS instrument is visible to the naked eye and indicates both that the electrical circuit is closed and that ionic re-distribution within the LEC active layer has occurred which would then be accessible via ToF-SIMS depth profiling.

2.3 Ion redistribution and salt dissociation equilibria in light-emitting electrochemical cells

The following section is a transcription of the publication:

M. Kawecki*, R.Hany, M.Diethelm, S.Jenatsch, Q.Grossmann, L.Bernard* and H.J. Hug; Direct Measurement of Ion Redistribution and ResultingModification of Chemical Equilibria in Polymer Thin Film Light-Emitting Electrochemical Cells; ACS Appl.Mater.Interf. 10, 39100 (2018)

The transcription was partially adapted in order fit the flow of the thesis.

Organic light emitting diodes (OLEDs) are becoming increasingly important for screens used in smart-phones, tablets, laptops and television, but also for room illumination applications. However, modern OLEDs are structurally complex devices consisting of multiple thin layers limiting their use for large area light-emission applications. [23] A much simpler organic light-emitting structure, the light-emitting electrochemical cell (LEC), [35,36] has been proposed by Pei et al. [37] already in 1995. A standard polymer LEC is a thin film device consisting of an emissive organic layer that contains an electrolyte, sandwiched between two electrodes. Recently, LEC devices delivering a bright luminance at 27.5 % external quantum efficiency have been presented. [38]

A large amount of work has been undertaken to explain the function of an LEC either by the electrodynamic [39,40] or the electrochemical [37,41,42,43,44] model: Slinker et al. [45] used electric force microscopy (EFM) to directly measure the electric field distribution across a planar LEC. They concluded that the potential distribution across the device is compatible with the electrodynamic model. Pei et al., [46] however, pointed out that the electrodynamic model was insufficient to fully describe the potential profiles measured by Slinker et al., and that an earlier study, [42] mapping the electric field profile across a planar LEC by the optical beam induced current (OBIC) method, showed a strong potential drop at the position of the emission zone. The formation of a p-i-n junction was later clearly confirmed by Matyba et al. [47] who combined scanning Kelvin probe microscopy (SKPM) with a local detection of the light emission, also on planar devices. The potential distribution across the device clearly favoured the electrochemical doping model. Later, van Reenen et al. [48] presented a unified description of LECs, where the electrodynamic and electrochemical models describe limiting cases; the simulation and experimental results showed that the electric field distributions predicted by the electrodynamic and electrochemical models occur in injection limited and non-injection limited devices, respectively. The occurrence of an electric field distribution compatible with a significant ion redistribution leading to the formation

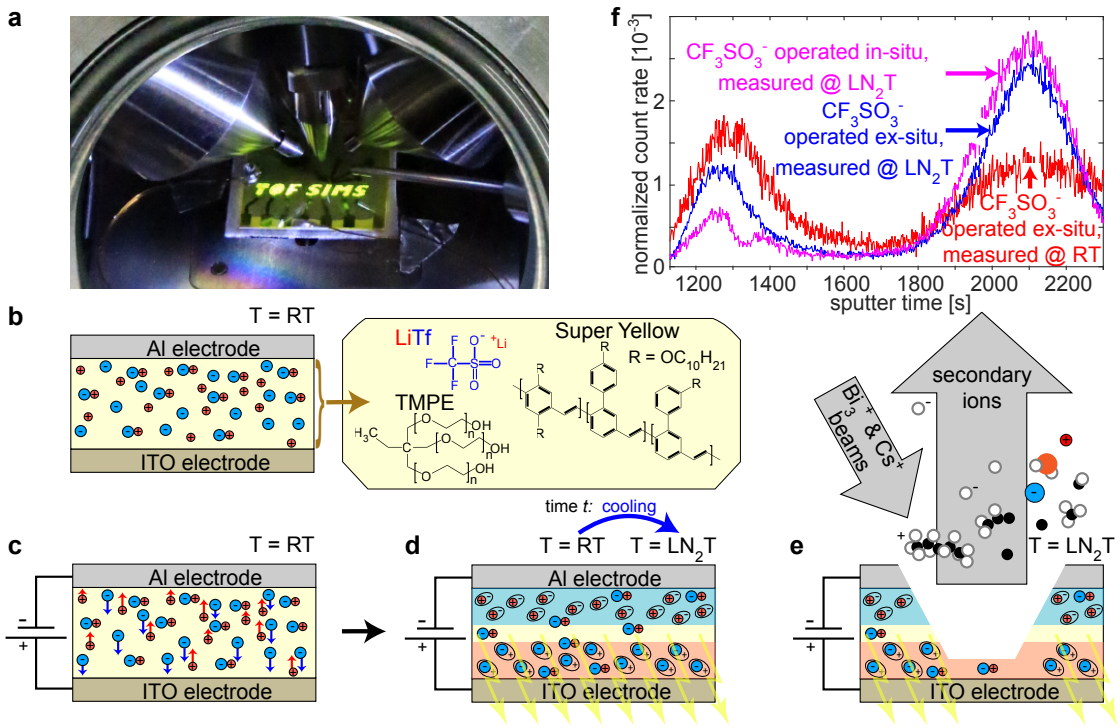

Figure 2.1: **Schematic diagram of the LEC functionality and experimental set-up for measuring ion distributions.** **a**, An LEC operated inside the ToF-SIMS. The top electrode was patterned to display the letters *TOF SIMS*. The ToF-SIMS primary ion gun, the ion extraction column, and the sputter gun are visible at the top of the image (from left to right). **b**, Schematics of the LEC device with Al top and ITO bottom electrode. **c**, LEC with forward bias (positive potential at the ITO electrode) immediately after the bias application: the anions/cations begin to redistribute towards the anode/cathode, respectively. **d**, status of the LEC after the time t. p-/n-doped layers have formed near the anode/cathode, respectively and light is emitted from the intrinsic region in between. The LEC is then cooled to liquid nitrogen (LN_2) temperature to suppress any successive ion motion. **e**, Schematic of the ToF-SIMS depth profiling process. **f**, $CF_3SO_3^-$ anion depth profiles after an operation time of 10 minutes, measured at room temperature (red curve), and at LN_2 temperature (blue curve), after disconnecting and transferring the device operated ex-situ into the ToF-SIMS. The magenta curve shows the anion depth profile measured after cooling an LEC operated (@RT) in-situ. The area under the curves is normalized to 1.

of a light-emitting p-i-n junction is thus established, at least for planar LEC structures. The direct quantitative detection of the ion distribution and assessment of the ion redistribution under typical device operation conditions for sandwich-type (layered) devices, however, remained an immense experimental challenge.

An experimental technique that can assess the distribution of atomic and molecular compositions across layered thin film structures to a depth of a few micrometers is time-of-flight secondary ion mass spectrometry (ToF-SIMS) combined with depth profiling. Sputter profiling, however, may strongly affect the ion distribution in LECs, and thus suppression of the ion mobility is necessary, for example by lowering the temperature or by chemical fixation using reactive ions. First measurements of the post-operation ion distribution in fixed and dynamic junction LECs were presented by Toshner et al. [49]. Depth profiles of CN^-, used as proxy for the molecular cation in a fixed junction LEC, confirmed the chemical ion immobilization during device operation and showed opposed ion distributions for opposed first-bias polarities. In contrast, in the dynamic junction LEC, profiles of the elemental Li^+ cation showed an accumulation at the bottom interface for all operation conditions, suggesting sputter-induced repulsion of the cations. Later, Shoji et al. [50] studied the same dynamic system while varying device thickness, salt concentration, operation bias and relaxation over time. Li^+ cations were directly measured while F^- served as proxy for the $CF_3SO_3^-$ anion. No redistribution of ions was observed for a bias of 5 V typically used for the operation of an LEC device, but a bias of 10 and 15 V resulted in substantially different profiles. When discussing the limitations, Shoji et al. show depth profiles performed once from the top Au electrode and once from the bottom ITO electrode on an unbiased device. In both cases a high Li^+ (respectively F^-) density was found at the corresponding bottom (resp. top) interface, indicating that the surface charging occurring during depth profiling pushes the mobile Li^+ cations to the bottom interface and attracts the anions to the top interface.

In both works [49,50] devices were biased ex-situ under an inert atmosphere and subsequently transferred inside the spectrometer. The time required for sample loading and instrument preparation resulted in a delay of around 2 h between

charging and depth profiling. ToF-SIMS measurements were performed at ambient temperatures. These experimental conditions affect both the quantitative and the qualitative value of the measured ion profile. First, ions can redistribute during the time required for sample loading (relaxation). Second, it is well documented [9] that the local surface charging that occurs during depth profiling produces large electric fields which drive ions mobile at room temperature to the top, respectively bottom, interface (depending on ion charge).

In our work we operate LECs with multiple sandwich structures *inside* a ToF-SIMS and conduct the sputter profiles at liquid nitrogen (LN_2) temperature. Figure 2.1**a** shows an example of an LEC structure with the top electrode patterned into the letters *TOF SIMS* operated inside the ToF-SIMS. As emitting material we used a phenyl-substituted poly(para-phenylenevinylene) copolymer termed Super Yellow (SY), the electrolyte was composed of the salt lithium trifluoromethanesulfonate ($Li^+CF_3SO_3^-$, LiTf) dissolved in a hydroxyl-capped oligoether, termed trimethylolpropane ethoxylate (TMPE). [51] Highly efficient and long-lived LECs have been demonstrated for this materials system, and for a constant current of 7.7 $mA\,cm^{-2}$ a current efficiency of 7.1 $cd\,A^{-1}$ and power efficiency of 5.9 $lm\,W^{-1}$ are reported. [52] The devices were operated in-situ at room temperature (RT) and at constant current with either forward or reverse bias and were cooled to LN_2 temperature after different operation durations (Figure 2.1**b-d**). Figure 2.1**b** displays the device state prior to bias application where the anions and the cations have the same distribution. Under bias, the cations begin to drift towards the negative and the anions towards the positive electrode (Figure 2.1**c**), leading to double-layer formation at the interfaces and facilitated charge injection. Further reorganization leads to the formation of p- and n-doped regions, at which point the devices were cooled down using a cold-finger in thermal equilibrium with a LN_2 bath (Figure 2.1**d**). After cooling, depth profiling was performed while the device driving current was maintained (Figure 2.1**e** - note that the light emission at the location of the sputter crater stopped as soon as the top electrode has been sputter-ablated). This procedure was developed to avoid relaxation and minimize the sputter-induced re-location of the ions inside the device that hindered the quantitative observation of the ion re-distribution in prior experiments. [50]

Figure 2.1**f** compares the $CF_3SO_3^-$ anion depth profiles measured at RT on devices operated ex-situ (red curve), measured at LN_2 temperature on devices operated ex-situ (blue curve), and measured at LN_2 temperature on devices operated in-situ (magenta curve). The devices were operated for 10 min at constant current and with positive bias at the bottom electrode prior to device disconnection (ex-situ measurements), respectively cooling onset (in-situ measurements). For ex-situ biased devices the time interval from bias disconnection to measurement onset (RT measurement), respectively cooling onset (LN_2 temperature measurement), was 60 min. The depth profiles measured at room temperature and after cooling to LN_2 temperature are noticeably different (compare red and blue lines in Figure 2.1**f**). This demonstrates that the ion distribution is modified considerably during depth profiling at room temperature, leading to a higher anion density at the top interface and consequently to an about 50% lower density near the bottom electrode. We attribute the accumulation of negative ions near the top interface to their attraction to the local positive charging at the upper surface during sputtering and ToF-SIMS operation. Interestingly, only a comparatively minor change of the ion density was found between devices biased in-situ and ex-situ when measured at LN_2 temperature (c.f. magenta and blue curves in Figure 2.1**f**). A quantitative analysis of the ion profiles reveals that the ion density at the bottom interface is only reduced by about 13% for the ex-situ biased device. This indicates that the space charge of the ions is well-screened, such that the space charge-induced fields, and consequently the restoring forces on the ions, remain small. Thus the ion relaxation (driven by diffusion) is much slower than the electric field drift-induced separation process. When the current bias is turned off, redistribution of the ions and dedoping occurs. In general, the device relaxation time depends on the LEC materials system and its composition; as one example, we mention small molecule organic salt LECs where the turn-on time to maximum luminance was measured to be on the order of one hour but the time required for full device relaxation was more than 60 hours. [53]

The distributions of the $CF_3SO_3^-$ for different operation conditions and for two devices with relative LiTf salt concentrations of 0.006 and 0.03, respectively, are

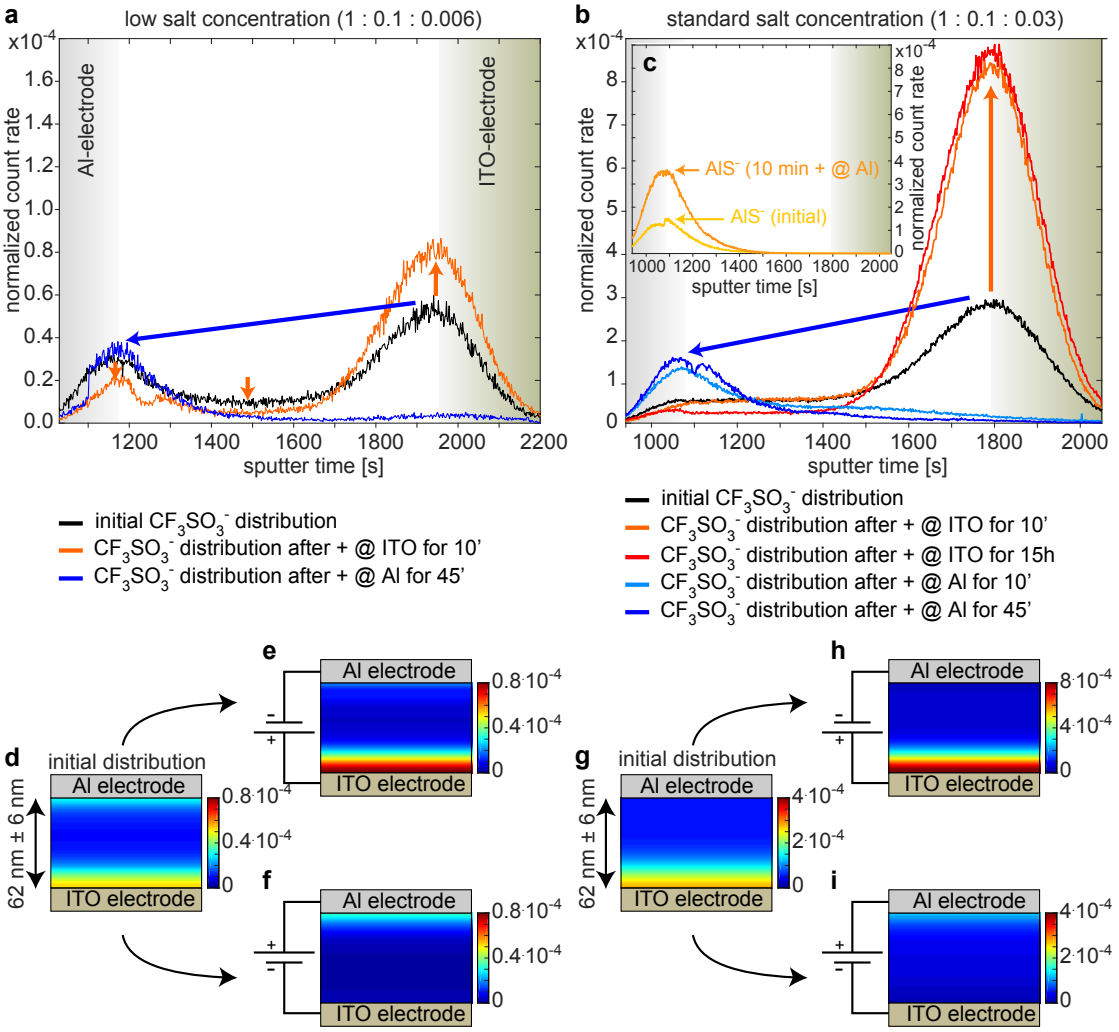

Figure 2.2: **Experimental anion distributions for in-situ operated devices.** **a**, Anion distribution across a low salt concentration LEC prior to bias application (black), and after 600 s operation in forward bias (orange) and in reverse bias (blue). **b**, Anion distribution across a standard salt concentration LEC prior to bias application (black), after 600 s and after 15 h operation in forward bias (orange and red curves, respectively), and in reverse bias after 600 s and 45 min (light blue and blue curves, respectively). **c**, Intensity of the AIS^- fragment in the standard salt concentration LEC prior to bias application (yellow) and after 600 s in reverse bias operation (light orange). **d** - **i**, Schematic representations of the ion distributions across the low and standard salt concentration LEC prior to bias application (**d** and **g**, respectively), after 600 s in forward bias operation (**e** and **h**, respectively) and after 600 s in reverse bias operation (**f** and **i**, respectively), as obtained from the depth profile data displayed in (**a**) and (**b**). All data were normalized to the independent CH^- count rate of the respective measurement.

displayed in Figure 2.2. The weight ratio SY : TMPE : LiTf = 1 : 0.1 : 0.03 (Figure 2.2**b**) is commonly considered as the optimized blend for maximum device performance. [51,54] Surprisingly, the initial anion distributions are inhomogeneous for both salt concentrations, with a peak near the bottom ITO electrode for both concentrations, and a smaller peak near the top Al electrode for the low salt concentration device (c.f. black curves of Figures 2.2**a** and **b** and color-coded spatial distribution of the ion densities depicted in Figures 2.2**d** and **g**). The higher anion density near the electrodes may arise from a phase separation process between the hydrophilic electrolyte (containing the salt and the ion-conductor TMPE) and the hydrophobic electroluminescent polymer, as previously found in other systems. [54,55,56,57,58,59] Phase separation can occur during spin-coating [56,58] or during film drying at elevated temperature [54] and the phase morphology can depend both on film thickness and ion concentration. [58] For standard and low salt concentration devices an operation with a *forward bias* (positive potential on bottom ITO-electrode) for 10 minutes leads to a shift of the anion distribution towards the ITO anode, whereas a *reverse bias* operation shifts the distribution towards the top electrode (cf. orange and red curves to the blue curves in Figure 2.2**a**, and **b**, respectively. Again, color-coded spatial distributions of the ion densities are depicted in Figures 2.2**e** and **f**, and Figures 2.2**h** and **i**). For the standard salt concentration sample we have also measured the anion distribution after 15 hours of operation with forward bias (red curve in Figure 2.2**b**). The density peak near the bottom electrode has further increased and the anion density in the bulk has further dropped.

Our results achieved on sandwich type devices show that the anion accumulation clearly shifts with bias application towards the respective positive electrode. This is compatible with the SKPM results of Matyba et al. [47] achieved on a planar LEC device, where the potential profile shifted with the direction of the applied bias. Our ToF-SIMS data, however, reveal a substantially increased anion count rate for forward bias operation: The comparison of the areas below the orange to the black curves in Figures 2.2**a** and **b** reveals that after operation with a forward bias for 10 minutes the total counts of the anions have increased by a factor of 1.12 and 2.12, respectively.

In a ToF-SIMS, the sample is locally bombarded with a primary ion beam (here Bi_3^+). The impact of the primary ion results in a complex collision cascade leading to the emission of secondary particles (molecules, molecular fragments and single atoms) specific to the local chemical composition of the sample. Among the emitted particles, a small fraction are ions. These secondary ions are accelerated by an applied electric field into the time-of-flight mass analyzer. We argue that the probability of the generation of secondary anions from the salt is much smaller than that arising from free anions not coordinated to lithium any more. While the first is a two-step process (desorption and ionization), the latter is simply an ion desorption process triggered by the energy release from the primary ion impact.

We thus conclude that the increased ion count rate detected by the ToF-SIMS after forward-bias device operation can be attributed to an increased total density of free anions in the LEC, and a correspondingly decreased number of anions coordinated to lithium. The forward bias operation thus leads to a re-adjustment of the salt⇌anion/cation equilibrium towards the ion side. A simple Gedanken-experiment explains why such a shift of the chemical equilibrium towards the free ion side is indeed expected: Application of a positive potential at the ITO bottom electrode will lead to a redistribution of the Li^+ ions towards the top and the Tf ions towards the bottom electrode, respectively. The local free ion concentrations near the bottom electrode, at position z_b in the device, then change from

$$\begin{aligned} C_{Li^+}(z_b, t_0) \quad &\text{and} \quad C_{CF_3SO_3^-}(z_b, t_0) \text{ to} \\ C_{Li^+}(z_b, t) = C_{Li^+}(z_b, t_0) - \Delta C_{Li^+}(z_b, t - t_0) \quad &\text{and} \quad C_{CF_3SO_3^-}(z_b, t) = \\ &\quad C_{CF_3SO_3^-}(z_b, t_0) + \\ &\quad \Delta C_{CF_3SO_3^-}(z_b, t - t_0)\,, \end{aligned}$$

and the concentrations near the top electrode, at position z_t in the device, change

from

$$
\begin{aligned}
& C_{\mathrm{Li^+}}(\mathrm{z_t}, \mathrm{t_0}) \quad \text{and} \quad C_{\mathrm{CF_3SO_3^-}}(\mathrm{z_t}, \mathrm{t_0}) \text{ to} \\
C_{\mathrm{Li^+}}(\mathrm{z_t}, \mathrm{t}) = C_{\mathrm{Li^+}}(\mathrm{z_t}, \mathrm{t_0}) + \Delta C_{\mathrm{Li^+}}(\mathrm{z_t}, \mathrm{t} - \mathrm{t_0}) \quad & \text{and} \quad C_{\mathrm{CF_3SO_3^-}}(\mathrm{z_t}, \mathrm{t}) = \\
& C_{\mathrm{CF_3SO_3^-}}(\mathrm{z_t}, \mathrm{t_0}) - \\
& \Delta C_{\mathrm{CF_3SO_3^-}}(\mathrm{z_t}, \mathrm{t} - \mathrm{t_0})\,.
\end{aligned}
$$

Here $C_{\mathrm{Li^+}}(\mathrm{z}, \mathrm{t_0})$ and $C_{\mathrm{CF_3SO_3^-}}(\mathrm{z}, \mathrm{t_0})$ denote the initial local cation and anion concentrations at a position z between the electrodes and at a time $\mathrm{t_0}$ prior to bias application. $C_{\mathrm{Li^+}}(\mathrm{z}, \mathrm{t})$ and $C_{\mathrm{CF_3SO_3^-}}(\mathrm{z}, \mathrm{t})$ denote the local concentrations at a time t after bias application and $\Delta C_{\mathrm{Li^+}}(\mathrm{z}, \mathrm{t} - \mathrm{t_0})$ and $\Delta C_{\mathrm{CF_3SO_3^-}}(\mathrm{z}, \mathrm{t} - \mathrm{t_0})$ denote the changes of the local concentrations arising from the electric field drift-induced redistribution of the ions occurring between time $\mathrm{t_0}$ and time t. Assuming locally $C_{\mathrm{Li^+}}(\mathrm{z_{b,t}}, \mathrm{t_0}) = C_{\mathrm{CF_3SO_3^-}}(\mathrm{z_{b,t}}, \mathrm{t_0})$, and $\Delta C_{\mathrm{Li^+}}(\mathrm{z_{b,t}}, \mathrm{t} - \mathrm{t_0}) = \Delta C_{\mathrm{CF_3SO_3^-}}(\mathrm{z_{b,t}}, \mathrm{t} - \mathrm{t_0})$, a simple calculation shows that the relations

$$
\begin{aligned}
& C_{\mathrm{Li^+}}(\mathrm{z_{b,t}}, \mathrm{t_0}) \cdot C_{\mathrm{CF_3SO_3^-}}(\mathrm{z_{b,t}}, \mathrm{t_0}) \quad > \\
& [C_{\mathrm{Li^+}}(\mathrm{z_{b,t}}, \mathrm{t_0}) \mp \Delta C_{\mathrm{Li^+}}(\mathrm{z_{b,t}}, \mathrm{t} - \mathrm{t_0})] \quad \cdot \left[C_{\mathrm{CF_3SO_3^-}}(\mathrm{z_{b,t}}, \mathrm{t_0}) \pm \Delta C_{\mathrm{CF_3SO_3^-}}(\mathrm{z_{b,t}}, \mathrm{t} - \mathrm{t_0})\right]
\end{aligned}
$$

hold for the positions $\mathrm{z_b}$ and $\mathrm{z_t}$. Thus, the local salt dissociation equilibria

$$
K = \frac{C_{\mathrm{LiCF_3SO_3}}(\mathrm{z_{b,t}}, \mathrm{t})}{C_{\mathrm{Li^+}}(\mathrm{z_{b,t}}, \mathrm{t}) \cdot C_{\mathrm{CF_3SO_3^-}}(\mathrm{z_{b,t}}, \mathrm{t})}
$$

re-adjust, further salt is decomposed at both electrodes, and the total free anion density in the device (the area below the orange and red curves in Figure 2.2**b**) is increased. Note that a recent model approach allows the consideration of changes of the chemical equilibrium, [60,61] but the influence of a bias on it has not been explicitly discussed nor demonstrated in an experiment.

Interestingly, the increase of the free ion density arising from the application of a forward bias is smaller for the low ion concentration sample (Figure 2.2**a**). This can be understood if the initial state of the salt dissociation equilibrium in

the samples without an applied electric field is considered. This equilibrium is connected to a further one, that is governed by the interaction of the cations with the oxygen sites of the TMPE molecules. [52] The TMPE-to-Li^+ concentration ratio affects the initial salt dissociation equilibrium. In the case of the low salt concentration sample, more of the cations are complexed by TMPE, driving the primary salt-to-ion equilibrium strongly towards the ion side. Then only little salt is available for further dissociation driven by electric field induced ion redistribution.

Further, it is surprising that the application of a *reverse bias* does not lead to an increase of the free anion density (area below the blue curve is reduced to about a third of the initial ion density), although a relocation of the anions towards the top electrode is clearly observed (see blue arrows in Figures 2.2**a** and **b**). This can be explained by the increase of the AlS^- peak near the top electrode (Figure 2.2**c**) that we ascribe to (electro-)chemical reaction products between Al and Tf. It has been demonstrated that Al is oxidized at a lower potential than the p-doping potential of the polymer. [62] In addition, it is well established from battery chemistry that Tf does not passivate and stabilize Al at higher potentials but causes severe corrosion. [63] The outcome of this is that a fraction of Tf is effectively consumed in side reactions and the detected anion density under reverse bias is decreasing.

The displacement of the anions during device operation can be correlated to measurements of the device performance. Figure 2.3 displays the time evolution of the luminance (green curves) and voltage required to drive the constant current of $5\,mA/cm^2$ (purple curves) for forward (Figure 2.3**a**) and reverse bias (Figure 2.3**b**), respectively, as well as the time evolution of the external quantum efficiency (EQE, number of photons emitted per electron) in forward bias operation (Figure 2.3**c**), calculated from the luminance curve (Figure 2.3**a**) and the device photoluminescence spectrum (Figure 2.3**d**). For forward bias operation the luminance increases roughly linearly for about 3 minutes, and then gradually approaches a saturation state within the next 45 minutes, compatible with the increase of the of anion density at the bottom electrode (Figure 2.2**b**). After 50 min the current efficiency reached $12.5\,cd\,A^{-1}$ and the power conversion efficiency $10.9\,lm\,W^{-1}$. Note that these efficiencies outperform reported values substantially. The main reason for

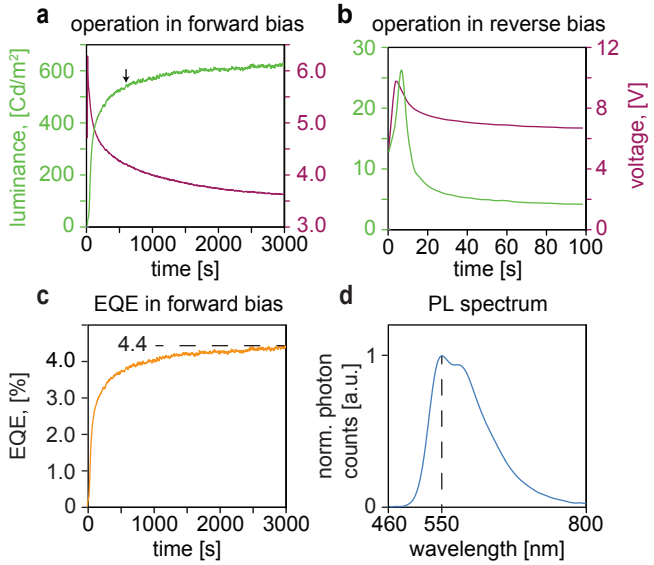

Figure 2.3: **LEC performance trends.** **a**, Luminance and voltage trend for forward bias operation. The black arrow denotes the 600 s measurement point from Figures 1f and 2. **b**, Luminance and voltage trend for reverse bias operation. **c**, External quantum efficiency (EQE) trend in forward bias operation. **d**, Device photoluminescence (PL) spectrum as used to calculate the EQE.

this is the (adjusted) reduced active layer thickness, which was 60 nm in our case compared to 100 nm in Ref. [52,54]. The active layer of an LEC is sandwiched between a metal electrode and a reflecting glass/ITO substrate, resulting in optical weak microcavity effects and a strong dependence of the luminance to the active layer thickness. [64]

For reverse bias, the luminance increased slightly and only during the first seconds but afterwards is completely quenched (Figure 2.3**b**). Again, this behaviour can be explained with the corrosion of the Al electrode, and it has been suggested that the electroluminescence is effectively quenched by Al^{3+} ions that are driven into the SY layer under *reverse bias*. Moreover, if reverse bias was followed by forward bias operation, the luminance did not recover to the values of a pristine forward-driven device and the required voltage remained high (data not shown). This demonstrates that the device under reverse bias is irreversibly degraded which is compatible with chemical reactions between the anion and the Al electrode, as detected by ToF-SIMS.

Summary

ToF-SIMS depth profiling was performed on sandwich LEC devices cooled to LN_2 temperature after different operation times and under forward and reverse bias. The results demonstrate that the in-situ operation and the use of cryogenic temperatures are required to suppress ion motion induced by the ToF-SIMS depth profiling measurement process, or a relaxation of the ion re-distribution after device operation. It was found that the initial ion distribution is not homogeneous through the 60 nm thick active layer and that a significant redistribution of the anions occurs during device operation. For a reverse bias operation, this anion redistribution is accompanied by a corrosion of the Al electrode and irreversible device degradation. For forward bias operation, a substantial increase of the total free anion density was found, which is attributed to a bias-induced change of the salt-to-ion chemical equilibrium. The presented work commends that inhomogeneous initial ion distributions and operation-dependent total ion densities must be considered in future work addressing device modelling. From an experimental point of view, an inhomogeneous and concentration-dependent initial salt distribution also implies that the transient turn-on kinetics must not necessarily speed up when the salt content is increased.

Materials and Methods

Fabrication of Super Yellow LECs in sandwich geometry. We followed the approach described in Ref. [51]. Dried (24 hours, 0.1 mbar, 160°C) lithium trifluoromethanesulfonate ($Li^+CF_3SO_3^-$, LiTf, Sigma-Aldrich), trimethylolpropane ethoxylate (TMPE, Sigma-Aldrich, average M_n 450) and Super Yellow (SY, Merck) were separately dissolved in tetrahydrofuran (THF, Sigma-Aldrich) in concentrations of 10 mg ml^{-1} (LiTf, TMPE) and 5 mg ml^{-1} (SY). These precursor solutions were then stirred for at least 6 h at 60°C. For the blend, the precursor solutions were mixed in mass ratios of 1:0.1:0.03 and 1:0.1:0.006 (SY:TMPE:LiTf) and were then stirred for at least 12 h at 60°C. Films were spin-coated at 2000 rpm inside a nitrogen-filled glovebox onto clean, pre-patterned ITO substrates and dried at

60°C for 1 h. Finally, aluminium top electrodes were thermally evaporated through a shadow mask defining cells with an active area of 3.1 or 7.1 mm^2. The organic layer thickness of 62 ± 6 nm was measured by profilometry.

Experimental ToF-SIMS setup. All depth profile measurements (apart from those displayed in Figure 1f) were performed with an IONTOF ToF-SIMS 5 instrument on LECs operated inside the ToF-SIMS's ultra-high vacuum chamber. Because depth profiling is a destructive process, samples with 8 aluminium top electrodes patterned onto a single ITO/glass substrate were used. LECs were driven at a constant current of 5 mA cm^{-2} using a Keithley 2400 sourcemeter. After a selected time, the device was cooled down from room temperature to liquid nitrogen temperature by means of a cold finger inside the instrument. The current remained applied during cooling and the required bias voltage and thus the device electrical resistance was monitored. The latter steadily increased when cooling was started, and reached a steady state between 6 and 6.5 V after about 10 min. From this we concluded that the final cryogenic temperature was reached. Each LEC cell was only biased once to exclude hysteresis effects.

ToF-SIMS data acquisition. The instrument was operated in the spectral mode using a 25 keV Bi^{3+} primary ion beam with an ion current of 0.6 pA to obtain a high mass resolution of around 5000. For depth profiling a 1 keV Cs^+ sputter beam with a current of 7 nA was used to remove material layer-by-layer in interlaced mode from a raster area of $600 \times 600\,\mu m^2$. This raster area was chosen to ensure a flat crater bottom over an area of $200 \times 200\,\mu m^2$ or $300 \times 300\,\mu m^2$ used for the mass-spectrometry. Depth profiling was started after cooling for 30 min. The inner aluminium and ITO electrode interfaces were defined by the half-maxima of the Al_2^- and In^- count rates. To account for possible minor current fluctuations during quantitative analyses, data shown in Figure 2.2 were normalised to the total CH^- count in the active layer. The CH^- fragment is evenly distributed throughout the active layer and did not saturate the detector. Measurements were repeated over multiple devices to assure full reproducibility.

Luminance measurements. For performance measurements, devices were placed in an airtight holder and were measured under nitrogen atmosphere outside the glove box at room temperature using a factory calibrated Konica Minolta LS-110 luminance meter with a close-up lens 110.

Photoluminescence spectrum acquisition. The LEC photoluminsecence spectrum was measured by fluorescence spectroscopy on a Horiba Jobin Yvon Fluorolog spectrofluorometer.

2.4 Observation of interfacial electric double-layer formation

In order to deepen the understanding of the dynamic processes that occur within organic LECs upon voltage application, measurements were conducted on devices with an active layer thickness of 430 nm[31] (compare to the 60 nm used in previous work conducted in the scope of this thesis[10]; see section 2.3). The increased device thickness can be expected to allow electric double layers, the *p*-doped and *n*-doped regions, and the emission zone to be better differentiated within the ToF-SIMS depth profiles. Further, these {SY : TMPE : LiTf = 1 : 0.1 : 0.03}-LECs were prepared with a silver top electrode[31]. Silver is more stable as electrode material than aluminum, which was used as material for the top electrode in previous work[31] (see Fig. 2.2), and allows prolonged device operation in *reverse bias*.

Measurements that were conducted on the 430 nm thick {SY : TMPE : LiTf = 1 : 0.1 : 0.03}-LECs covered with a silver top electrode and operated in *reverse bias* show a narrow anion peak building up at the top electrode (Fig. 2.4). This sharp interfacial peak is distinct from the bulk accumulation of the anion, which also increases with operation duration. The occurrence of the interfacial accumulation is in agreement with the formation of electric double layers at the electrode interface. However, several uncertainties remain. Firstly, no such sharp interfacial peak was visible in the measurements conducted on 60 nm thick LECs with an aluminium top electrode (Fig. 2.2). The absence of such a peak in *reverse bias* operation can be explained by anion degradation at the aluminium interface. The absence of a distinct peak in *forward bias* operation can be explained by the known porosity of evaporated aluminium electrodes which leads to the accumulation of roughness during depth profiling, and may have resulted in insufficient resolution at the bottom ITO electrode. Secondly, note that in Fig. 2.4, a minor peak at the top

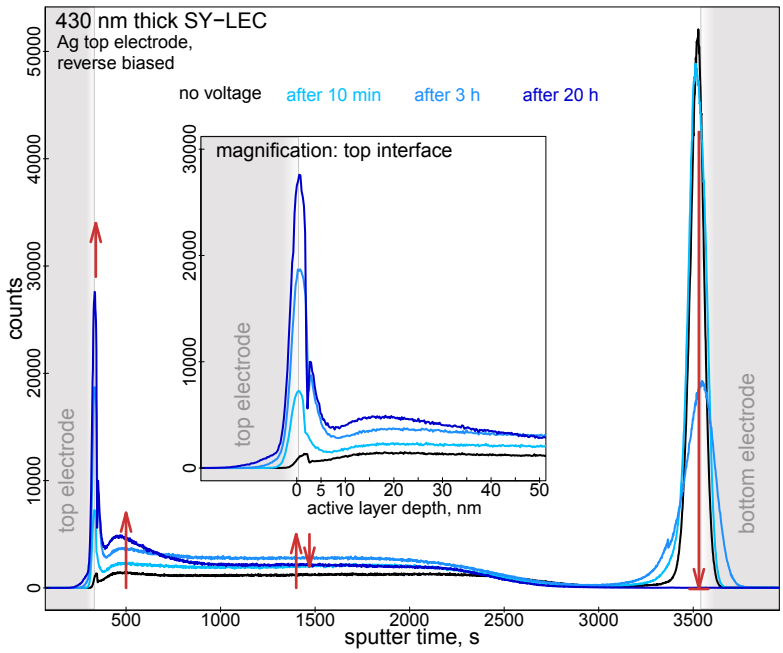

Figure 2.4: **430 nm thick SY-LEC with Ag top electrode operated in *reverse bias*.** Anion distribution across an optimized salt concentration SY-LEC prior to bias application (black), and after 10 min (light blue) 10.5 h (blue) and 20 h (dark blue) operation in *reverse bias*. **Inset:** Magnification of the top 50 nm. The sputter time has been converted to depth within the organic active layer by means of profilometric measurements of the total layer thickness and under the assumption of a homogeneous sputter yield across the active layer.

interface also appears in the measurement conducted without any applied voltage (black line). This peak can be explained by minor interfacial anion accumulation induced by the positive charging of the top electrode during sputter- and primary ion impact.

The measurements plotted in Fig. 2.4 are part of the following published work:

M. Diethelm, A. Schiller, M. Kawecki, A. Devizis, B. Blülle, S. Jenatsch, E. Knapp, Q. Grossmann, B. Ruhstaller, F. Nüesch and R. Hany*; *The dynamic emission zone in sandwich polymer light-emitting electrochemical cells*; Adv. Funct. Mater., 1906803 (2019)

2.5 Suggested improvements for the study of dynamic processes in thin film electronics

The presented study contains, to the best of the authors knowledge, the first mass spectrometric measurements probing in-situ the dynamical processes occurring across an operating thin film electronic device. The aim of this section is to make the reader aware of the current methodological limitations and briefly discuss two areas were substantial improvement can be achieved: **a)** in the streamlining of the measurement procedure, and **b)** in the measurement time resolution.

a) In order to conduct the measurements presented in sections 2.3 and 2.4, existing ToF-SIMS instrumentation was adapted. The electric feed-through allowing for temperature control in the ToF-SIMS 5 instrument stationed at Empa Dübendorf was used to operate the LEC devices in-situ. These were mounted on a commercially available sample holder designed for temperature controlled measurements (Fig. 2.5). The temperature controlled ToF-SIMS sample holder has only a total of four electrical connections. Two of the connections are used for the temperature sensor and only two are available for LEC device operation. For the acquisition of the profiles shown in sections 2.3 and 2.4, the LEC devices were mounted individually for each measurement (see sample mounting in Fig. 2.5). Under these conditions, typically between one to two thirds of the experimenting time are required by sample handling, sample transfer, and the in-situ cooling process. If more electrical connections to the exchangeable, coolable sample holder could be implemented, several devices could be operated successively, thus significantly decreasing the experimenting time.

Further, for the acquisition of the profiles shown in sections 2.3 and 2.4, the electical connection between sample holder and LEC device was achieved by individually gluing the wires to the LEC electrodes using silver paste (labelled in Fig. 2.5 as 'electrical contacts to sample electrodes'). ToF-SIMS measurements are conducted at vacuum pressures in the range of 10^{-8} mbar. To reduce pumping times and ease of handling, it is suggested to adapt the sample holder to contain in-built electrical contacts that can be clamped down on the device studied.

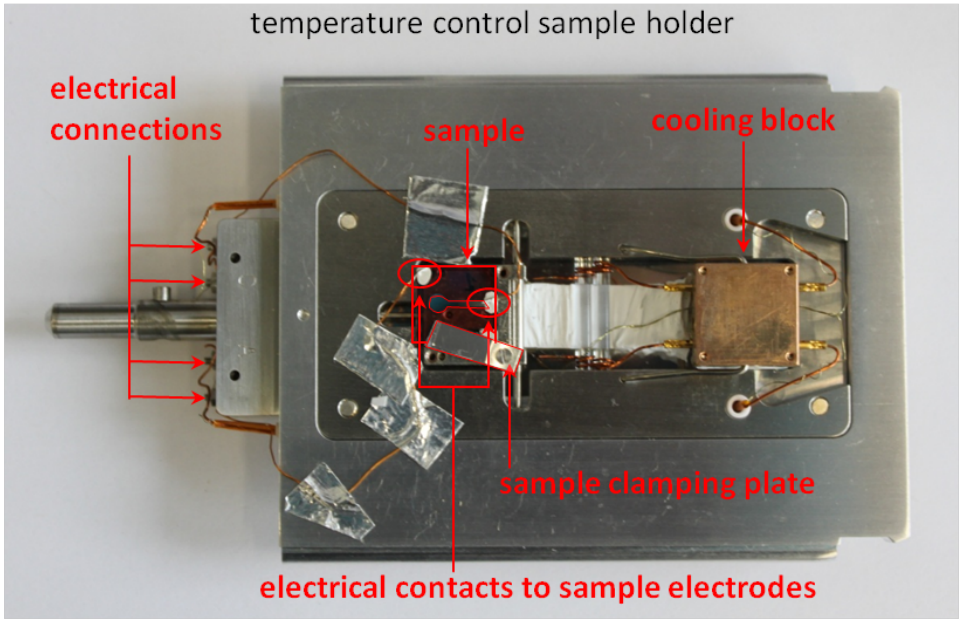

Figure 2.5: **ToF-SIMS temperature control sample holder with mounted electronic device.**

b) The time resolution with which dynamic processes can be studied in operating electronic devices by means of ToF-SIMS is limited by the time it takes to cool down an operating device to a temperature at which the processes of interest are frozen. In the presented measurements, the sample was cooled by physical contact of the sample holder with a LN_2-cooled cooling finger that is pressed against the spring-loaded cooling block of the sample holder. With this set-up, the migrations of the molecular ion CF_3SO_3 in {SY-TMPE-LiTF} LECs could be sufficiently suppressed within approximately 15 minutes, which can hence be considered as the time resolution obtained in the experiments here (sections 2.3 and 2.4). In biology, studies of synaptic vesicle release require time resolutions in the order of milliseconds and dedicated cooling approaches have been developed for this purpose. In particular, Heuser et al. demonstrated that muscle tissue can be frozen within 1 ms after application of a timed electrical impulse[65]. In their study, the sample is pressed against a metal block cooled with liquid helium. Alternatively a timed electric pulse can also be correlated with the plunging of a sufficiently thin

sample into a cryogenic liquid. This latter freezing approach cannot be conducted in vacuum. However, the design of a setup to rapidly freeze a sample ex-situ in a protected atmosphere and then transfer it in the cooled state to a pre-cooled ToF-SIMS sample holder appears feasible. The measurements in this thesis were conducted in-situ, but, for the LECs studied, it was observed that if the device is disconnected and maintained at cryo-temperature no noticeable relaxation takes place. From this it is concluded that the measurements[10,31] shown in section 2.3 and section 2.4 could also have been performed on devices operated and cooled ex-situ, provided the devices could be transferred in cooled state to the ToF-SIMS and kept at low temperatures.

2.6 ToF-SIMS study of perovskite solar cells and perovskite LEDs

Perovskite-based solar cells are currently among the most efficient photovoltaic technologies in laboratory conditions. The theoretical efficiency limit for an ideal *p-n* junction solar cell with a band gap energy close to the optimum is approximately 33 %[66]. In the course of the last decade, the attained power conversion efficiency of single-junction perovskite solar cells increased from 3.8 % in the year 2009 to a power conversion efficiency of 25.2 % for the currently certified record, as of November 2019[67]. In comparison, the currently certified record for single-crystal silicon solar cells is a power conversion efficiency of 26.1 %[67]. However, the certified power conversion efficiency record for silicon solar cells has improved only by approximately 2 % since the year 1995[67], suggesting that the attainable optimum for silicon solar cells is gradually being approached.

The bandgap energy of a solar cell defines at what wavelengths light will be absorbed most efficiently. By changing the composition and stochiometry of the perovskite absorber layer in a perovskite solar cell, its bandgap energy can be tuned to a value between 1.1 and 1.9 eV[68]. Changes to the perovskite lattice structure are reported to allow bandgaps up to 3.1 eV to be reached[69]. Multi-junction solar cells, consisting of a stack of multiple single-junction absorber layers, allow the

theoretical maximum power conversion efficiencies that govern single-junction cells to be exceeded. The ability to adapt the bandgap energy of single-junction perovskite absorber layers and the efficiencies reached by single-junction perovskite solar cells, make perovskite solar cells one of the most promising current photovoltaic technologies.

Before market implementation of perovskite-based solar cells can be considered, however, operational hysteresis[70] and degradation processes leading to short shelf- and life-times[28] have to be addressed. Further, the fabrication processes that had been developed for laboratory purposes are not suitable for the fabrication of solar cells with a large surface area. Technologies for the fabrication of large-surface area, high-efficiency perovskite solar cells have yet to be developed[71].

2.6.1 The perovskite crystal structure and perovskite solar cells

The term *perovskite* commonly refers to any material with a crystal structure analogue to the one of calcium titanium oxide ($CaTiO_3$), which is the namesake for this crystal family. A perovskite crystal has the stochiometry ABX_3 (Fig. 2.6a), where A and B are two cations, A being much larger than B, and X is an anion bonding to both cations. What renders the perovskite crystal structure unique is its flexibility when it comes to tailoring the material properties[72,73]. Trihalide perovskites in which the role of A is taken by the organic molecules methylammonium (MA) or formamidinium (FA) demonstrate both high photoabsorbtion and photoemission properties and electron and hole diffusion lengths exceeding 1 µm[73].

A simple single-junction perovskite solar cell consists of a planar perovskite absorber layer sandwiched between a p-type charge extraction layer (hole extraction) and an an n-type charge extraction layer (electron extraction) (Figure: perovskite solar cell structure schematic (Fig. 2.6b)). This stack of three layers is in turn sandwiched between two electrodes. An incoming photon is absorbed in the perovskite absorber layer and excites an electron and a hole into a weakly bound

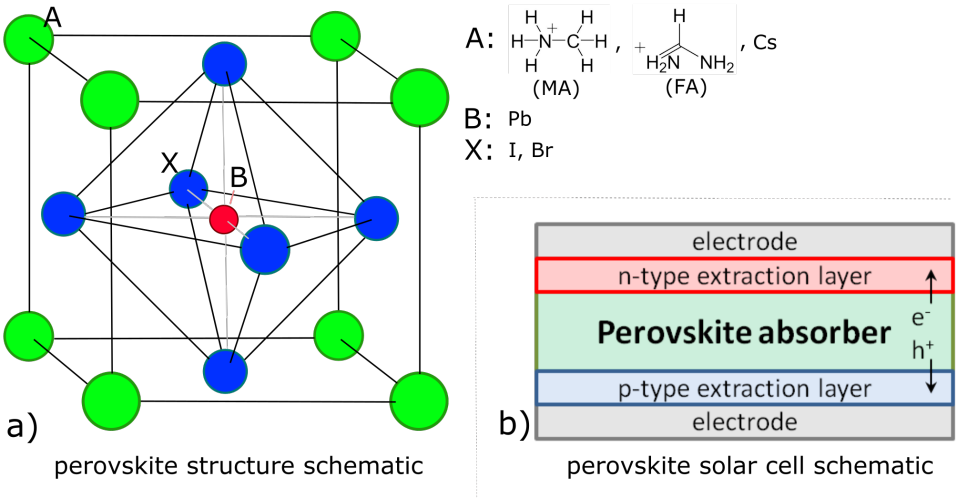

Figure 2.6: **Perovskite crystal structure and schematics of a perovskite solar cell. a)**The ABX_3 -type perovskite crystal structure. In the case of perovskite solar cells, the cation B is most often lead, while iodide and bromine are used for the anion X and the role of A is taken by the organic cation methylammonium (MA, $CH_3NH_3^+$) or formamidinium (FA, $CH_5N_2^+$). **b)** Schematics of a simple single-junction perovskite solar cell.

state. The potential difference between the two charge extraction layers drives the electron and hole separation.

In the course of this thesis, ToF-SIMS measurements were conducted for external research groups on perovskite absorbers and emitters. Three of these collaborations resulted in high-impact publications[33,28,32] and are highlighted below.

2.6.2 Collaboration with the group of Prof. H. J. Snaith (Oxford Univ.): Towards stable perovskite solar cells

The research group of Prof. Henry J. Snaith, in a project[33] led by Dr. Sai Bai, used a perovskite photoabsorber with the composition $(FA_{0.83}MA_{0.17})_{0.95}Cs_{0.05}Pb(I_{0.9}Br_{0.1})_3$, where FA stands for formamidinium and MA for methylammonium. The perovskite absorber was sandwiched between a nickel oxide (NiO) *p*-type charge-extraction layer and a [6,6]-phenyl-C_{61}-butyric acid methyl ester (PCBM) *n*-type charge extraction layer (Fig. 2.7a). A Cr/Cr_2O_3 buffer layer was implemented be-

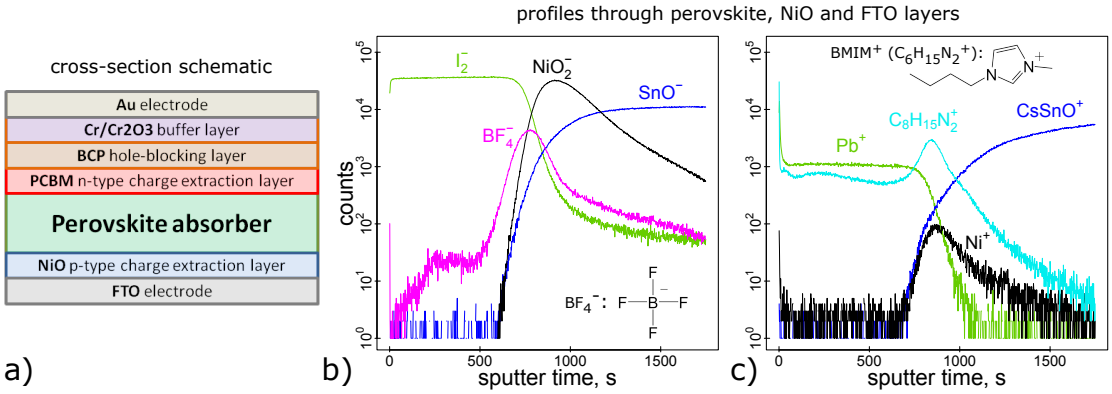

Figure 2.7: **Distribution of BMIM and BF_4 in a planar perovskite absorber layer. a)** Schematics of the solar cell architecture as used in the study by Bai et al. **b)** Negative polarity depth profile across the perovskite absorber layer (characteristic ion: I_2^-), the NiO p-type charge extraction layer (characteristic ion: NiO_2^-)and into the fluorine-doped tin oxide (FTO) covered substrate (characteristic ion: SnO^-). The distribution of the BF_4^- anion is visible in magenta. **c)** Positive polarity depth profile through the same device layers. Pb^+ is the characteristic ion for the perovskite absorber layer, Ni^+ for the charge extraction layer, $CsSnO^+$ for the FTO substrate and the $C_8H_{15}N_2^+$ secondary ion corresponds to the unfragmented BMIM cation. **Note:** ToF-SIMS depth profiles were conducted not across complete devices, but only the perovskite absorber layer and the layers below. Panels b) and c) are adapted from[33].

tween the silver electrode and the remaining stack of the solar cell. The inclusion of a Cr/Cr_2O_3 buffer layer is known to reduce the corrosion of the current collector[74,75]. A layer of Bathocuproine (BCP) was included as hole-blocking layer between the Cr/Cr_2O_3 buffer layer and the PCBM n-type charge extraction layer.

Among the main current limitations of perovskite solar cell technology is the rapid degradation of the perovskite absorber when compared to established technologies. The project led by Dr. Bai followed the observation that the addition of ionic liquids into the perovskite absorber layer can, but does not have to, significantly improve the life time of perovskite solar cells under constant exposure to heat and light. The aim of the study was to understand the conditions under which addition of an ionic liquid impacts the device life time. In particular, it is reported that the addition of the ionic liquid 1-butyl-3-methylimidazolium tetrafluoroborate ($BMIMBF_4$) to the perovskite absorber layer results in perovskite solar cells that

drop to 80 % of their peak performance only after an estimated 5'200 hours under full spectrum sunlight at 70-75°C.[33] The aim of the ToF-SIMS measurements conducted in the course of this collaboration was to assess the distributions of the cation and anion across the perovskite absorber layer. ToF-SIMS dual beam depth profiling was not conducted across full solar cell stacks as seen in Fig. 2.7a, but only the perovskite absorber deposited on the NiO *p*-type charge extraction layer. The PCBM, BCP, Cr/Cr_2O_3, and Au layers had not been deposited in order to maximize the depth resolution across the perovskite layer in the depth profiles acquired by Tof-SIMS.

For the devices containing the ionic liquid $BMIMBF_4$, ToF-SIMS measurements showed that $BMIMBF_4$ ion pairs accumulate at the perovskite/NiO interface, while only the BMIM cation is distributed throughout the bulk (Fig. 2.7b and c). It is suggested that the BMIM cations are excluded from the perovskite crystal due to their size. Excluded cations that are not already bound to an anion may bind to sites at surface and grain boundaries which are otherwise vulnerable to oxidation and moisture adsorption. It is this mechanism that is brought forward to explain the observed suppression of device degradation.

This collaboration led to the following publication:

S. Bai, P. Da, C. Li, Z. Wang, Z. Yuan, F. Fu, M. Kawecki, X. Liu, N. Sakai, J.T.-W. Wang, S. Huettner, S. Buecheler, M. Fahlman, F. Gao and H.J. Snaith; *Planar perovskite solar cells with long-term stability using ionic liquid additives*; Nature **571**, 245-250 (2019)

2.6.3 Collaboration with the group of Dr. F. Fu (Empa): Understanding degradation pathways in perovskite solar cells

Dr. Fan Fu and coworkers studied both formamidinium and methylammonium lead-iodide-based perovskite absorbers with the aim to determine degradation pathways responsible for efficiency loss and fatal device failure upon exposure to light and heat[28]. In the course of the study led by Dr. Fu, perovskite solar cells, exposed perovskite absorber layers, and PbI_2, which is a degradation product of lead-iodide-based perovskite, were exposed to full sunlight spectrum illumination at a temperature of 80°C in an N_2 atmosphere. The temperature was regulated by a copper heating plate. Solar cells were aged under standardized 1 sun illumination, bare perovskite absorbers under 0.1 sun illumination (Fig. 2.8a). The microstructure and chemical composition of the films and film surfaces were characterized by means of scanning and transmission electron microscopy (SEM and TEM, respectively), energy dispersive X-ray spectroscopy (EDX), X-ray diffraction (XRD) and ToF-SIMS. The aim of the ToF-SIMS measurements conducted in the course of this collaboration, was to assess changes in chemistry across both solar cells and exposed perovskite abosorber layers before and after the heat-light treatment. The following publication is based on this collaboration:

F. Fu, S. Pisoni, Q. Jeangros, J. Sastre-Pellicer, M. Kawecki, A. Paracchino, T. Moser, J. Werner, C. Andres, L. Duchene, P. Fiala, M. Rawlence, S. Nicolay, C. Ballif, A. N. Tiwari and S. Buecheler; *I2 vapor-induced degradation of formamidinium lead iodide based perovskite solar cells under heat-light soaking conditions*; Energy & Environmental Science **12**, 3074-3088 (2019)

In degraded devices, scanning electron microscopy images conducted across the perovskite layer revealed increasing porosity with increasing exposure to heat and light. The scanning electron microscopy results indicate that the degradation does not progress from the grain boundaries inwards, but rather starts in the grain bulk ([28], Fig 3, Fig S8). Further, thermogravimetric analysis combined with quadrupol mass spectrometry ([28], Fig S9) suggest loss of gaseous I_2 as a by-product of the

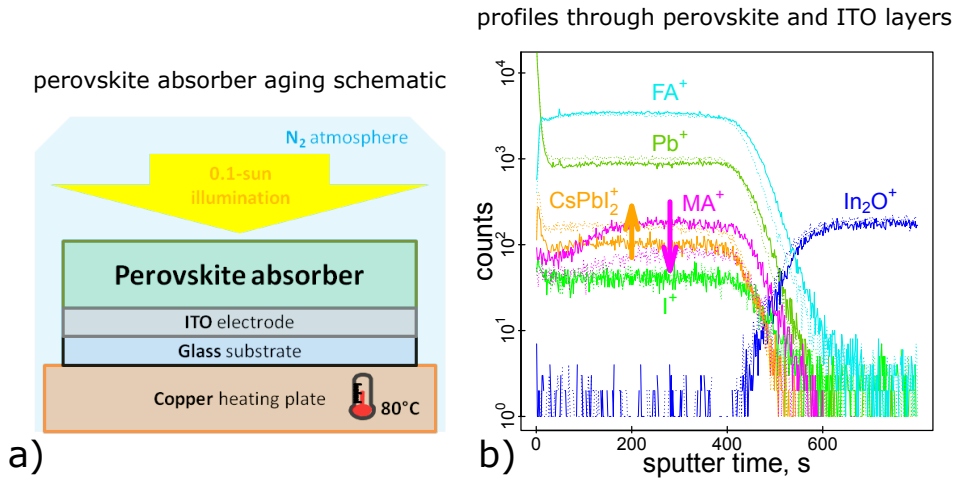

Figure 2.8: **Perovskite absorber degradation under exposure to heat and light.** **a)** Schematic of a perovskite absorber and the conditions for accelerated degradation. **b)** ToF-SIMS depth profile before and after degradation. The solid lines correspond to a positive polarity depth profile conducted on a pristine $FAPbI_3$:MABr ($10\,mg\,ml^{-1}$) perovskite absorber deposited on ITO. The dotted lines correspond to a depth profile measurement conducted on an identical absorber layer, but after exposure of the absorber to 0.1 sun illumination by white LEDs in a N_2 filled glovebox and on a 80°C heating plate, over a duration of 10 h. The profiles plotted in panel b) were acquired on perovskite absorbers that were not capped by any further thin film layers. Panel b) is adapted from[28]

degradation of the perovskite layer. The increasing porosity of the degraded perovskite layer, as observed by scanning electron microscopy, is hypothesized to originate from I_2 vapor loss and observed to lead in the long-term to a rupturing of the device layers through internal pressure build-up. ToF-SIMS Cs-dual beam depth profiling through degraded and intact perovskite absorbers shows a drop in signal attributed to the organic cation methylammonium (MA^+), and an intensity increase for the $CsPbI_2^+$ secondary ion in degraded perovskite absorbers (Fig. 2.8b). These results are in accordance with the loss of the cation MA^+ from the perovskite absorber layer and a decomposition of the perovskite absorber to PbI_2. A decomposition of the perovskite absorber to PbI_2 would result result in the emission of I_2 vapor as observed in the thermogravimetric analysis combined with quadrupol mass spectrometry.

2.6.4 Collaboration with the group of Prof. F. Gao (Univ. Linköping): Understanding molecular passivation in perovskite LEDs

The group of Prof. Feng Gao, in a project[32] led by Dr. Weidong Xu, used a formamidinium (FA)-based lead-iodide perovskite crystal ($FAPbI_3$) as emitter in perovskite LEDs. In a perovskite LED, electrons and holes are not extracted at two opposing interfaces of the perovskite layer but injected. Within the perovskite layer radiative electron-hole recombination then can take place. However, lattice defects provide pathways for non-radiative recombination which result in thermal losses in perovskite LEDs. The introduction of organic molecules which interact with the defect sites can diminish non-radiative recombination. However, little is known on the relation between molecular structure and passivation efficiency. It is this relation that the study led by Xu et al. aims to establish. (Note: contrary to the studies by Bai et al.[33] (section 2.6.2) and Fu et al.[28] (section 2.6.3), the study by Xu et al. does not discuss degradation of the perovskite film but addresses purely the LED device efficiency.)

The LED architecture (Fig. 2.9a) used in this study consists of a $FAPbI_3$ per-

ovskite emitter layer, a TFB (poly(9,9-dioctyl-fluorene-co-N-(4-butylphenyl)diphenylamine)) hole injection layer, and an electron injection layer consisting of zinc oxide (ZnO) nanocrystals and polyethylenimine ethoxylated (PEIE). ITO (indium tin oxide) is chosen for the transparent electrode. Molybdenum oxide/gold (MoO_x/Au) is chosen for the other electrode.

Xu et al. systematically varied the ability to from hydrogen bonds in a defect passivating molecule added to the perovskite layer, and documented the efficiency of a perovskite LED as a function of this property[32]. It was found that efficient passivation requires the passivating additive to bind to free lead sites at perovskite crystal edges in order to prevent the lead from acting as an electron trap, a mechanism leading to non-radiative decay. Eliminating free lead atoms as electron sinks increases the overall device efficiency in regards of radiative electron-hole recombination. It was observed by Xu et al. that to achieve this effect, the ability of the passivating additive to form hydrogen bonds needs to be weakened such that the probability to bond with the organic cation of the perovskite drops below the probability of the electrone lone-pairs of the passivating molecule to form a coordinative bond with the lead cation. In the passivating molecules used by Xu et al., the electron lone pairs were situated on a nitrogen atom. The formation of coordination bonds with Pb_2^+ was shown by FTIR (Fourier-transform infrared spectroscopy) and clearly correlated with the device efficiency. The role of ToF-SIMS in this collaboration was to keep track of the distributions of the passivating molecules across the perovskite layer (Fig. 2.9b) and the main conclusions of this study were inferred from the efficiency trends and modelling. In order to maximize the depth resolution across the perovskite layer in the depth profiles acquired by Tof-SIMS, profiling measurements were conducted across uncapped perovskite emitter layers, not the full perovskite LED stack.

This collaboration led to the following publication:

W. Xu, Q. Hu, S. Bai, C. Bao, Y. Miao, Z. Yuan, T. Borzda, A.J. Barker, E. Tyukalova, Z. Hu, M. Kawecki, H. Wang, Z. Yan, X. Liu, X. Shi, K. Uvdal, M. Fahlman, W. Zhang, M. Duchamp, J.-M. Liu, A. Petrozza, J. Wang, L.-M. Liu, W.

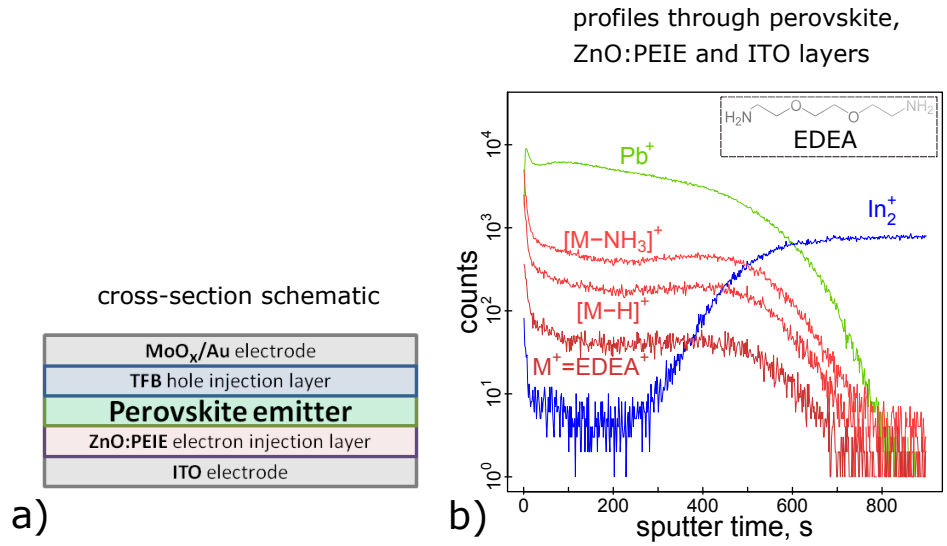

Figure 2.9: **Perovskite light-emitting diode passivation. a)** Schematics of the LED architecture as used in the study by Xu et al. **b)** Distribution of the passivation molecule 2,2'-(ethylenedioxy)diethylamine (EDEA) across a perovskite emitter deposited on ZnO:PEIE/ITO substrate. Throughout the study by Xu et al., the ability of the amine end-groups to engage in hydrogen bonding was tuned by symmetric addition and subtraction of oxygen atoms in the molecule center, as well as variation of the carbon chain length between the amine end-groups and the nearest oxygen atom. Note, the reduced depth resolution in the ToF-SIMS depth profile is a result of the high porosity of the perovskite emitter. This figure is adapted from [32]

Huang and F. Gao; *Rational molecular passivation for high-performance perovskite light-emitting diodes*; Nature Photonics **13**, 418-424 (2019)

3 Supramolecular SIMS

3.1 Introduction

Supramolecular interactions were shown in the previous chapter (section 2.6.4) to be decisive for efficient passivation of perovskite thin film electronics. In organic electronics, non-covalent interactions also impact intramolecular electronic coupling and with it the electron and hole mobilities across entire organic layers[76]. In biology, non-covalent interactions govern, for example, molecular recognition[77] and encode the folding of proteins[78]. The field of supramolecular chemistry covers the study of non-covalent interactions that lead to the formation of multi-molecular structures.

The established measurement techniques used to asses supramolecular interactions in biological and organic matter are solid state nuclear magnetic resonance (ssNMR)[79], X-ray diffraction (XRD)[80], and electron microscopy (cryoEM)[81]. However, unless the molecular interactions lead to self-assembly visible on scales of an electron microscope, such as is the case for lipid double-layers, molecular interactions can only be probed under the constraints of high chemical purity (ssNMR, cryoEM) or structural periodicity (XRD).

Secondary ion mass spectrometry is not constrained by the requirements of chemical purity or structural perioidicity. The detection and analysis of supramolecular secondary ions opens the door for spatially resolved identification of molecular interactions in organic and biological matter, and for the investigation of the statistical molecular surroundings of chosen molecules.

The interactions that are of interest in supramolecular chemistry include hy-

drogen bonding, the family of π-interactions, Van der Waals Forces, and electrostatic interactions. In this chapter, the focus is on hydrogen bonding and pi-interactions. The systems studied include the proteinogenic amino acids and a set of monosachharides which are two groups of biological building blocks known to interact through hydrogen bonding. Further, supramolecular dimers of 2-(2-naphthyl)ethylamine are detected, a molecule that does not form hydrogen bonds with itself but engages in dipole-π interactions. In order to increase the complexity of the system in a controlled manner, mixtures of 2,5-piperazinedione, a small hydrogen bonding molecule, and dextran, a polysachharide, are studied. For all systems probed, the thicknesses of the films studied exceed the domain of molecular monolayers.

Mass spectrometry using electrospray ionization (ESI), is successfully used in the study of non-covalent ligand-receptor[82] or protein-protein[83,84] interactions. The potential of ESI has been recently expanded to the study of complex membrane protein assemblies[85]. To date, however, the mass spectrometric study of molecular interactions and supramolecular structures is limited to liquid[82,83,85], or solution processed[86] sample material. Hard ionization techniques, such as secondary ion mass spectrometry (SIMS), which allow solid matter to be studied, result in pronounced molecular fragmentation and are commonly considered too energetic to preserve multi-molecular ions. Contrary to the common perception, as early as 1979, supramolecular secondary ions detected from solid nitrogen (N_2) probed at the temperature of 15 K were observed, and clusters up to $[N_2]_{22}^+$ were reported[87]. Soon after, ion impact-induced chemical reactions leading to complicated cluster chemistries were reported for solid N_2O, NO, N_2O_3 and N_2O_4 probed with heavy monoatomic primary ions, which led to the conclusion that the composition of extracted clusters need not be indicative of the composition of the solid[88]. From today's perspective, these observations seem to have discouraged any potential further research into the extraction of intact supramolecular clusters by means of SIMS. Meanwhile, instrumentation evolved and in particular cluster primary ion sources emerged[11,12] which are less prone to induce fragmentation and chemical reactions upon primary ion impact.

3.2 Supramolecular secondary ions in the spectra of amino acids and monosaccharides

The mass spectra of all 21 proteinogenic amino acids contain peaks that could be assigned to supramolecular secondary ions. Here, the mass spectra of one of these amino acids, L-proline, shall be described in detail. The positive time-of-flight (ToF) SIMS spectrum acquired on a drop-deposited film of L-proline is shown in Fig. 3.1A. The strong peak at mass 116.07 u corresponds to unfragmented proline molecules, ionized through acceptance of a positive hydrogen ion. Further major peaks occur at masses corresponding to $[nM+H]^+$, where n is an integer larger than 1, M the molecular mass of proline and H the mass of hydrogen. In the negative spectrum, a similar pattern is observed, with strong intensities for masses that correspond to $[nM-H]^-$ (Fig. 3.1B). In the positive proline spectrum (Fig. 3.1A), the intensity of the $[11M+H]^+$ and $[12M+H]^+$ peaks is stronger than the intensity of the $[9M+H]^+$ and $[10M+H]^+$ peaks, and $n>12$ supramolecular secondary ions are absent. This pattern indicates that proline arranges on the surface into closed supramolecular clusters of 12 proline molecules each. The intensity of the $[11M+H]^+$ peak exceeds the intensity of the $[12M+H]^+$ peak which is in line with the positive ionization of a closed 12-proline cluster by loss of a single $[M-H]^-$ molecular ion. A similar pattern of peaks has been previously observed in ESI proline mass spectra, suggesting that proline forms closed clusters of 12 molecules during the liquid-gas transition of evaporating micro-droplet[89]. Simulations conducted in that study confirm the ability of proline to form a closed, 12-molecular, icosahedral structure[89]. The ToF-SIMS results presented reveal that proline can arrange into closed 12-molecular icosahedrons also upon bulk solidification. In the negative proline spectrum a $[13M-H]^-$ proline peak is observed (Fig. 3.1B), which is tentatively attributed to 12-molecular proline assemblies ionized by the interaction with a negatively charged $[M-H]^-$ proline molecular ion.

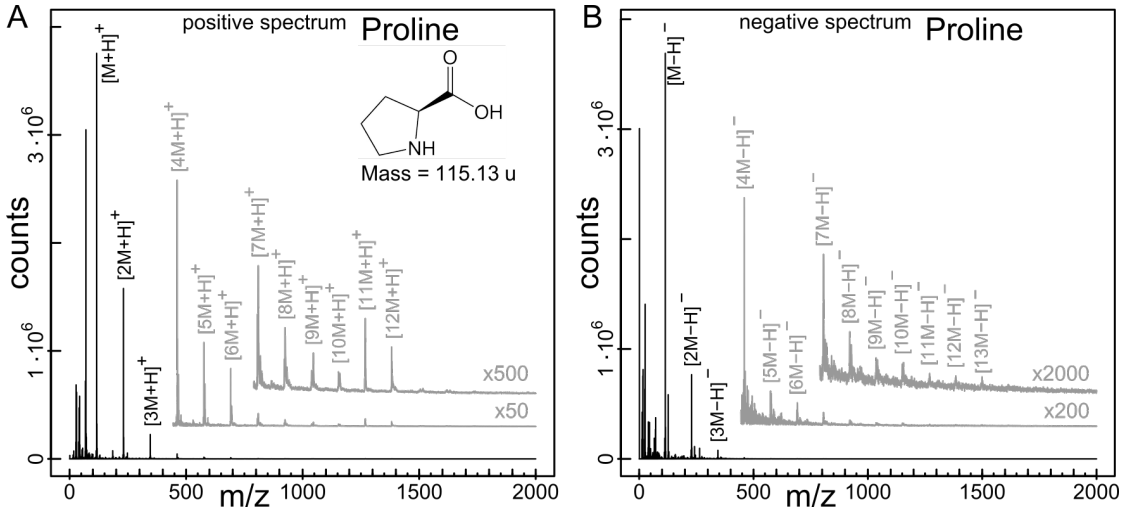

Figure 3.1: **ToF-SIMS mass spectra acquired on L-Proline in positive and negative polarity. (A)** ToF-SIMS positive polarity spectrum of pure L-proline drop-deposited on a silicon wafer. **(B)** ToF-SIMS negative polarity spectrum of pure L-proline drop deposited on a silicon wafer. The spectrum was acquired on the same sample as the positive polarity spectrum presented in panel A.

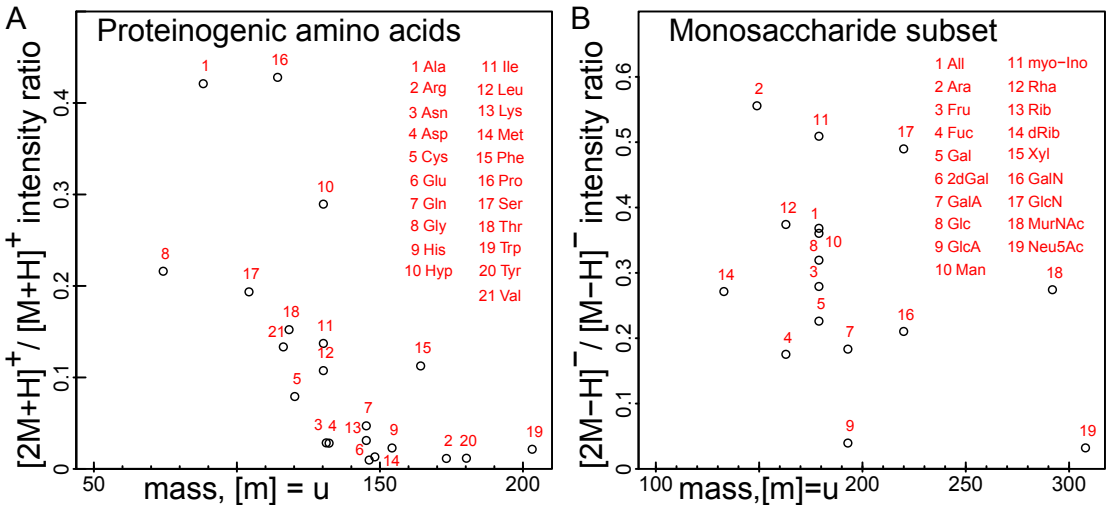

Figure 3.2: **Detection probabilities for supramolecular dimer secondary ions in different amino acids and monosaccharides.** **(A)** Counts of supramolecular dimers normalized to unfragmented monomer counts and plotted versus mass for all proteinogenic amino acids, each deposited individually on a separate silicon wafer.**(B)** Counts of supramolecular dimers normalized to unfragmented monomer counts and plotted versus mass for a set of 19 monosaccharides, each deposited on a separate silicon wafer. Note, in most monosaccharides, unfragmented molecular ions are observed to preferentially form through loss, not acquisition, of a proton (H^+).

The mass spectra of all 21 proteinogenic amino acids contain peaks assigned to $[nM+H]^+$ or $[nM-H]^-$. In all these mass spectra, $[nM\pm H]^\pm$ patterns are observed, as opposed to, for example, $[nM-(n-1)(H_2O)\pm H]^\pm$ or $[nM-(n-1)H_2\pm H]^\pm$ patterns which would emerge from chemical reactions to form covalent bonds. Therefore, the monomer units of the secondary ions consisting of n amino acids are held together by non-covalent attractive interactions. When comparing all proteinogenic amino acids, it was found that the count ratio of the peak corresponding to the dimer ($[2M+H]^+$) over the peak corresponding to the unfragmented molecular ion ($[M+H]^+$) varies (Fig. 3.2A). With increasing molecular mass, the $[2M+H]^+/[M+H]^+$ intensity ratio tends to decrease for amino acids. This trend appears less pronounced for the dimer peaks found in monosaccharide mass spectra (Fig. 3.2B). Whereas amino acids can be expected to interact at a single point of contact via a single or double hydrogen bond, monosaccharides are able to form hydrogen bonds between the saccharide faces. The trend in the $[2M+H]^+/[M+H]^+$ intensity ratios in amino acids suggests that the probability of a supramolecular dimer to not decay in the extraction process depends on the ratio of the bonding strength between the two molecules to the forces acting on that bond arising from the specific type of supramolecular vibrations. With increasing molecular masses, the energy stored in a vibrational mode involving the two molecules of a supramolecular dimer will increase. It can be expected, that the forces acting on a non-covalent bond between the two molecules thus increase as well with increasing molecular masses. In molecules that interact via multiple points of contact, such as is the case for monosaccharides, forces due to supramolecular vibrations will not necessarily act on all points of contact simultaneously in a disruptive manner.

3.3 Supramolecular secondary ions held together by interactions weaker than hydrogen bonding

In dry amino acids, the strongest non-covalent interactions occur through hydrogen bonds. Other non-covalent interactions are also observed to lead to $[nM+H]^+$-type peaks. For example, despite 2-(2-naphthyl)ethylamine not forming hydrogen bonds with itself, a high-intensity $[2M+H]^+$ peak is detected in the positive

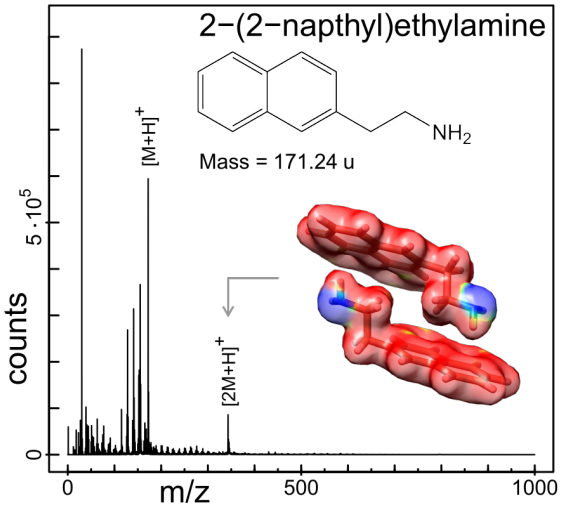

Figure 3.3: **ToF-SIMS positive polarity spectrum of pure 2-(2-napthyl)ethylamine.** The modelled conformation of the supramolecular dimer is depicted as inset, showing a density isosurface at 0.02 a.u. colored with the electrostatic potential, blue being negative (min. value: -0.02 Eh/e); red positive (max. value: 0.025 Eh/e)

polarity spectra acquired on drop-deposited 2-(2-naphthyl)ethylamine (Fig. 3.3). Quantum chemistry simulations conducted using the range-separated Meta-GGA functional M11[90] with full structural optimization indicate that the most stable conformation of two 2-(2-naphthyl)ethylamine molecules is through dipole-π non-covalent bonding (Fig. 3.3, inset), resulting in an interaction strength of -0.40 eV. The benchmark for detectable non-covalent interactions was set by the ToF-SIMS measurements conducted in 1979 on N_2 condensed on a copper substrate cooled to a temperature of 15 K, where positively charged cluster secondary ions of N_2 were reported[87]. Quantum chemistry simulations conducted in the scope of this thesis estimate the binding energy, dominated by London forces, between two N_2 molecules to be -0.02 eV.

3.4 2,5-piperazinedione and the enhanced formation of supramolecular ribbons in the presence of dextran

2,5-piperazinedione is capable of forming double hydrogen-bonds at two opposing sites, and is known from X-ray diffraction to form ribbons of linear supramolecular polymers during crystallization[91,92]. Here, 2,5-piperazinedione is used in order to study a system with a higher degree of supramolecular polymerization. A positive mass spectrum acquired on a drop deposited film of 2,5-piperazinedione is shown in Fig 3.4A.

It is observed by means of optical microscopy that the morphology of the 2,5-piperazinedione film is different in the center, at the spot where the droplet contracted when drying, than on the remaining surface. A positive mass spectrum acquired at the center spot is shown in Fig 3.4B. The supramolecular peaks have a higher intensity at the center of the spot, suggesting increased alignment. Measuring on pure 2,5-piperazinedione, it is observed that beyond a threshold primary ion dose density limit, the intensities of the 2,5-piperazinedione $[nM+H]^+$ peaks rapidly drop below the level of noise (see Fig.3.4C). The vanishing of $[nM+H]^+$ peaks with accumulated ion impact damage confirms that the supramolecular secondary ions do not form in a process of rearrangements induced by the primary ion impact, but are directly related to the supramolecular structure of the bulk. Note, only measurements acquired at primary ion dose densities below the degradation onset are compared in the other figures in this study.

In order to study the detection of supramolecular secondary ions in complex organic matter, while maintaining control over the chemical composition of the system, 2,5-piperazinedione is diluted in dextran, a polysaccharide. Figure3.4D shows the positive polarity spectrum of a drop-deposited film consisting of dextran (Mn=5'000 u) and 2,5-piperazinedione in a mass ratio of 5:1. Despite the dilution of the 2,5-piperazinedione, the high intensity peaks in the mass spectrum are still dominated by the characteristic $[nM+H]^+$ pattern observed in Fig.3.4A. However,

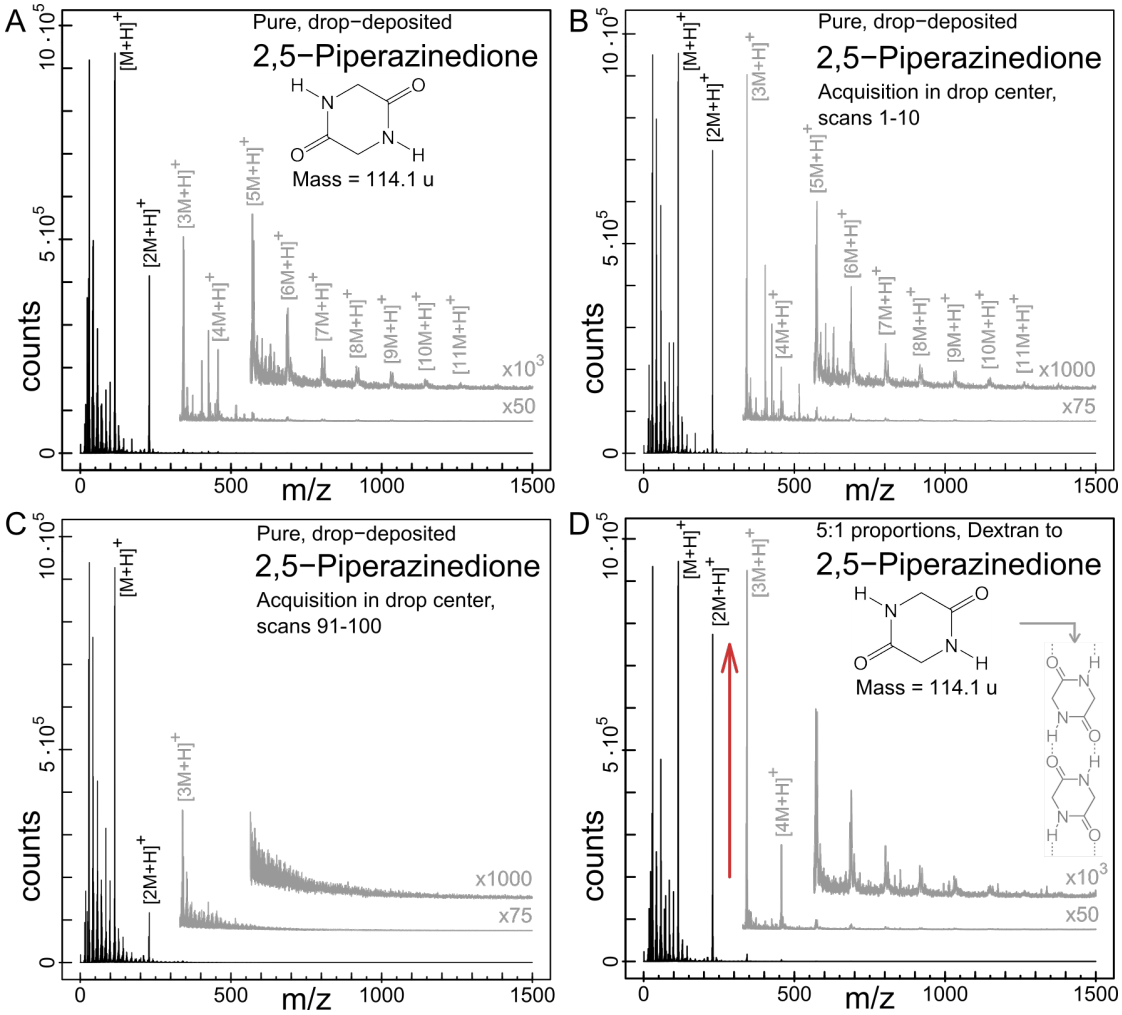

Figure 3.4: **ToF-SIMS positive polarity spectra acquired on systems containing 2,5-piperazinedione. (A)** ToF-SIMS positive polarity spectrum of pure 2,5-piperazinedione. **(B)** ToF-SIMS positive polarity spectrum of pure 2,5-piperazinedione acquired at the center of a drop-deposited film. It is ovserved in optical microscopy that the morphology of the 2,5-piperazinedione film is different in the center, at the spot where the droplet contracted when drying, than on the remaining surface. **(C)** The influence of accumulated primary ion impact damage on the positive polarity ToF-SIMS spectrum of 2,5-piperazinedione. The spectra plotted in panels B and C are part of the same measurement, acquired over a duration of 100 scans on a 100x100 μm^2 area with a raster resolution of 128x128 pixels. Panel C presents the spectrum summing the last 10 scans (scans 91-100, average ion dose density per scan: $8.0{\cdot}10^{12}$ ions/cm^2) - Panel B presented the spectrum summing the first 10 scans (scans 1-10, average ion dose density per scan: $4.6{\cdot}10^{11}$ ions/cm^2). The intensity ratio of the $[2M+H]^+$ peak to the monomer unit peak ($[M+H]^+$) diminishes from 0.76 in the average over the first 10 scans to 0.13 in the average over the last 10 scans of the 100 scan measurement. **(D)** ToF-SIMS positive polarity spectrum of 2,5-piperazinedione in dextran (Mn=5000 u) in the total mass ratio 1:5.

with the dextran present (Fig.3.4D), the intensity ratios of the successive $[nM+H]^+$ 2,5-piperazinedione peaks normalized to the monomer unit peak ($[M+H]^+$) are $1:0.82:0.019:0.0047:0.00082$ for n$\in\{1\text{-}5\}$, whereas on pure 2,5-piperazinedione (Fig.3.4A) these intensity ratios are $1:0.55:0.015:0.0038:0.00062$. The increase in normalized $[nM+H]^+$ peak intensities indicates that the presence of dextran reinforces the alignment of 2,5-piperazinedione into supramolecular linear polymers. Organic molecules are known to segregate according to the structure of the associated hydration layer. This is the phenomenon behind aqueous biphasic solutions[93,94]. This phenomenon can also be the explanation behind the partitioning of dextran and 2,5-piperazinedione molecules, which were deposited in H_2O. Such exclusion will preferentially separate the more hydrophobic supramolecular 2,5-piperazinedione polymers, rather than individual molecules of 2,5-piperazinedione, from dextran. The selectivity of the partitioning process can be envisioned to drive the alignment of 2,5-piperazinedione into supramolecular oligomers.

3.5 Probing molecular interaction probabilities in systems consisting of multiple different molecules

The extraction and detection of assemblies consisting of weakly bound molecules can provide insight into the chemical surroundings of a selected molecule in a complex organic environment. Information on the probability that a molecule M_i and a molecule M_j will non-covalently interact is contained in the $[M_i+M_j+H]^+$ ion count. Assuming that the extraction (p_{ij}^{ext}), ionization (p_{ij}^{ion}), transmission (p_{ij}^{tra}) and detection (p_{ij}^{det}) probabilities for a weakly bound pair (M_i+M_j) were known, the number of such (M_i+M_j) pairs on the surface probed can be related to the the $[M_i+M_j+H]^+$ counts as follows:

$$n_{ij} = \alpha^{-1} \cdot \frac{[M_i + M_j + H]^+}{p_{ij}^{ext} \cdot p_{ij}^{ion} \cdot p_{ij}^{tra} \cdot p_{ij}^{det}} \tag{3.1}$$

Here, n_{ij} =:$n(M_i{+}M_j)$ is the total number of $(M_i{+}M_j)$ pairs within the area probed, and α is the surface fraction affected by primary ion impact.

May in the following a system be considered that consists of only two types of molecules, M_1 and M_2. In this binary system, a molecule of the type M_1 can either interact with a molecule of the type M_2, or with a different M_1 molecule. The fraction X_{12}^1 of M_1 molecules that, out of these two possible options, interacts with an M_2 molecule can be expressed by the following equation:

$$\begin{aligned} X_{12}^1 &= \frac{n(M_1+M_2)}{n(M_1+M_2)+n(M_1+M_1)} \\ &= \frac{\frac{[M_1{+}M_2{+}H]^+}{p_{12}^{ext}\cdot p_{12}^{ion}\cdot p_{12}^{tra}\cdot p_{12}^{det}}}{\frac{[M_1{+}M_2{+}H]^+}{p_{12}^{ext}\cdot p_{12}^{ion}\cdot p_{12}^{tra}\cdot p_{12}^{det}}+\frac{[2M_1{+}H]^+}{p_{11}^{ext}\cdot p_{11}^{ion}\cdot p_{11}^{tra}\cdot p_{11}^{det}}} \end{aligned} \tag{3.2}$$

In the nomenclature chosen, the superscript in X_{12}^1 denotes the molecule whose interactions are of interest (here M_1) and the subscript denotes the two specific interaction partners, one of which is the one denoted in the superscript. The secondary ion counts for $[M_1{+}M_2{+}H]^+$ and $[M_1{+}M_1{+}H]^+$ are acquired in one single spectrum. (Note, the value of X_{12}^1 is independent of the surface fraction affected by primary ion impact, α.) A priori, extraction, ionization, transmission and detection probabilities are not known. In a first approximation, the extraction, transmission, and detection probabilities are considered equal for all supramolecular dimers of comparable mass and bond strength. Equation 3.2 then becomes:

$$X_{12}^1 \approx \frac{\frac{[M_1{+}M_2{+}H]^+}{p_{12}^{ion}}}{\frac{[M_1{+}M_2{+}H]^+}{p_{12}^{ion}}+\frac{[2M_1{+}H]^+}{p_{11}^{ion}}} \tag{3.3}$$

The ionization probabilities are, however, considered to depend on the supramolecular pairing. The ionization probability of an extracted $(M_i{+}M_j)$ pair can be estimated from the ion count of its individual molecules as:

$$\begin{aligned} p_{ij}^{ion} &\approx p_i^{ion}+p_j^{ion} \\ &= \frac{[M_i+H]^+}{c_i\cdot p_i^{ext}\cdot p_i^{tra}\cdot p_i^{det}}+\frac{[M_j+H]^+}{c_j\cdot p_j^{ext}\cdot p_j^{tra}\cdot p_j^{det}}, \end{aligned} \tag{3.4}$$

where $c_{i,j}$ are the molecular concentrations on the sample surface and must be known or determined by a suitable experimental method. Using Equation 3.4, Equation 3.3 becomes:

$$X_{12}^{1} \approx \frac{\frac{[M_1+M_2+H]^+}{[M_1+H]^+/(c_1 \cdot p_1^{ext} \cdot p_1^{tra} \cdot p_1^{det}) + [M_2+H]^+/(c_2 \cdot p_2^{ext} \cdot p_2^{tra} \cdot p_2^{det})}}{\frac{[M_1+M_2+H]^+}{[M_1+H]^+/(c_1 \cdot p_1^{ext} \cdot p_1^{tra} \cdot p_1^{det}) + [M_2+H]^+/(c_2 \cdot p_2^{ext} \cdot p_2^{tra} \cdot p_2^{det})} + \frac{[2M_1+H]^+}{2[M_1+H]^+/(c_1 \cdot p_1^{ext} \cdot p_1^{tra} \cdot p_1^{det})}} \quad (3.5)$$

Considering the extraction, transmission and detection probabilities equal for molecules of comparable mass, analogue to the approximation made before for supramolecular dimers, Equation 3.5 is reduced to:

$$X_{12}^{1} \approx \frac{\frac{[M_1+M_2+H]^+}{([M_1+H]^+/c_1 + [M_2+H]^+/c_2)}}{\frac{[M_1+M_2+H]^+}{([M_1+H]^+/c_1 + [M_2+H]^+/c_2)} + \frac{[2M_1+H]^+}{([M_1+H]^+/c_1 + [M_1+H]^+/c_1)}} \quad (3.6)$$

If now in the two-molecular model system the concentrations of M_1 and M_2 are known, Equation3.6 can be used to estimate the fraction of molecules M_1 that interact with a molecule M_2 and the fraction of molecules M_1 that interact with its own kind. Extending Equation 3.6 to a system consisting of n molecules of comparable masses results in:

$$X_{ij}^{i} \approx \frac{\frac{[M_i+M_j+H]^+}{([M_i+H]^+/c_i + [M_j+H]^+/c_j)}}{\sum_n \frac{[M_i+M_n+H]^+}{([M_i+H]^+/c_i + [M_n+H]^+/c_n)}}, \quad (3.7)$$

In the framework of the assumptions made, equations of the type 3.7 can be used to estimate the interaction partner distribution for a molecule of interest M_i by analysis of its supramolecular dimer secondary ions.

In order to investigate this approach towards the determination of molecular interaction partner distributions, a model system consisting of the small molecules glycine, asparagine and 2,5-piperazinedione in the molar ratio 1:1:1, drop deposited as a film on clean, plasma-treated silicon, was used. All three of these molecules interact through hydrogen bonds. The positive spectrum acquired on the above system is plotted in Fig. 3.5. The intensities of the peaks of interest (see Fig. 3.5)

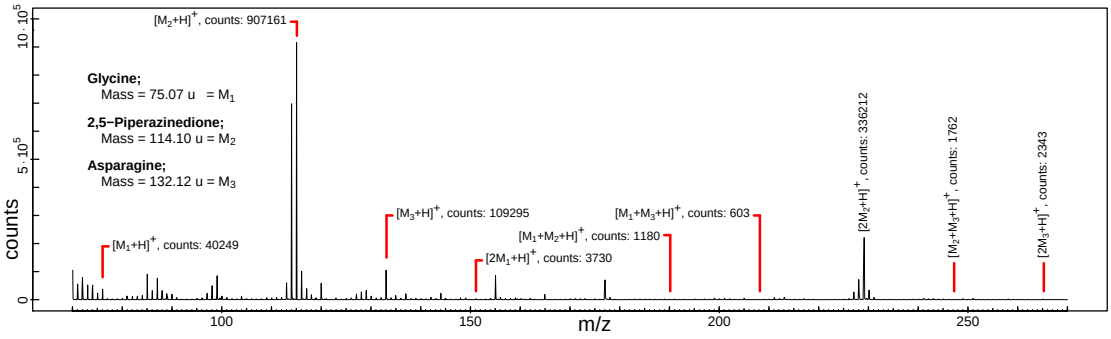

Figure 3.5: **Positive polarity spectrum acquired on a film consisting of glycine (Gly), 2,5-piperazinedione (2,5-P.) and asparagine (Asp).**

$[Gly+H]^+$	$[[2,5\text{-}P.]+H]^+$	$[Asp+H]^+$	$[2Gly+H]^+$	$[2[2,5\text{-}P.]+H]^+$	$[2Asp+H]^+$	$[Gly+[2,5\text{-}P.]+H]^+$	$[Gly+Asp+H]^+$	$[[2,5\text{-}P.]+Asp+H]^+$
40249	907161	109295	3730	336212	2343	1180	603	1761

Table 3.1: **Total counts for monomer and dimer peaks in a thin film consisting of glycine (Gly), 2,5-piperazinedione (2,5-P.) and asparagine (Asp).** The counts were integrated over the full peak width. Note, the $[Gly+Asp+H]^+$ peak is below the noise floor as defined by the height intensity of the surrounding 1 u periodic peaks. In Fig. 3.6 the $[Gly+Asp+H]^+$ dimer formation probability is considered as zero for the bar plot computation and the integrated count rate (here red) of the peak occurring at the $[Gly+Asp+H]^+$ position is accounted for within the error bars in Fig. 3.6.

are shown in Table 3.1. For each of the three molecules in the drop-deposited film consisting of glycine (Gly), asparagine (Asp) and 2,5-piperazinedione (2,5-P.) in the molar ratio 1:1:1, the interaction partner distribution (expressed in percent) is shown in Table 3.2 and calculated for different normalization assumptions which are described in the table caption. The data shown in Table 3.2 is plotted in Fig 3.6. The bar height indicates the interaction partner distributions as calculated by means of Equation 3.7. The error bars indicate the range of values obtained based on the different assumptions made as shown in Table 3.2. Based on the normalized $[M_i+M_j+H]^+$ supramolecular dimer intensities, the qualitative conclusion is that each of the three molecules has a strong preference to associate with its own kind. This conclusion is independent of the specific normalization assumptions.

A	Gly	2,5-P.	Asp
Gly	67.66 %	21.40 %	10.94 %
2,5-P.	0.35 %	99.13 %	0.52 %
Asp	12.81 %	37.42 %	49.77 %

B	Gly	2,5-P.	Asp
Gly	89.78 %	2.41 %	7.81 %
2,5-P.	0.66 %	98.42 %	0.92 %
Asp	24.46 %	10.51 %	65.03 %

C	Gly	2,5-P.	Asp
Gly	89.78 %	2.41 %	7.81 %
2,5-P.	0.38 %	98.70 %	0.92 %
Asp	12.57 %	9.46 %	77.97 %

F	Gly	2,5-P.	Asp
Gly	75.97 %	24.03 %	0 %
2,5-P.	0.35 %	99.13 %	0.52 %
Asp	0 %	42.92 %	57.08 %

E	Gly	2,5-P.	Asp
Gly	97.38 %	2.62 %	0 %
2,5-P.	0.66 %	98.42 %	0.92 %
Asp	0 %	13.92 %	86.01 %

D	Gly	2,5-P.	Asp
Gly	97.38 %	2.62 %	0 %
2,5-P.	0.37 %	98.70 %	0.92 %
Asp	0 %	10.82 %	89.18 %

Table 3.2: **Interaction partner distributions for glycine (Gly), 2,5-piperazinedione (2,5-P.) and asparagine (Asp). (A,D)** Interaction partner distributions as computed purely from the $[M_i+M_j+H]^+$ peak intensities by $X^i_{ij} := 100\cdot[M_i+M_j+H]^+/\sum_n([M_i+M_n+H]^+)$, where X^i_{ij} is the estimated percentage of supramolecular dimers containing molecule M_i that also contain molecule M_j. **(B,E)** Interaction partner distributions as computed taking molecular ionization probabilities into account (Equation 3.6): $X^i_{ij} := 100\cdot([M_i+M_j+H]^+/([M_i+H]^+ + [M_j+H]^+))/(\sum_n([M_i+M_n+H]^+)/([M_i+H]^+ + [M_n+H]^+))$. Note, this normalization implicitly assumes that the ionization potential of a supramolecular dimer is a function of the ionization potentials of its components, however, the hydrogen bonds present in the dimer influence the ability of the dimer to accept a proton. **(C,F)** Interaction partner distributions as computed taking molecular ionization probabilities into account and making a tentative assumption on the mass dependence of the extraction probabilities. (This calculation is conducted with the sole aim to estimate the dependence of results on assumptions made.) The mass-dependence of the extraction probability (p^{ext}) is approximated here from the $[2M+H]^+/[M+H]^+$ count ratio trend of the proteinogenic amino acids, as plotted in Fig. 3.2A. For dimers consisting of two different molecules, the assumption is made here that it is the mass of the smaller molecule that defines the force acting on the non-covalent bond in supramolecular vibrational modes. Based on the mass dependence of the $[2M+H]^+/[M+H]^+$ peak ratios in the amino acids, the following extraction probabilities are set: for dimers where glycine is the smallest molecule, $p^{ext}=0.35$; for dimers where 2,5-piperazinedione is the smallest molecule $p^{ext}=0.2$; for dimers where asparagine is the smallest molecule $p^{ext}=0.15$. $X^i_{ij} := 100\cdot([M_i+M_j+H]^+/([M_i+H]^+ + [M_j+H]^+)*p^{ext}_{ij})/(\sum_n([M_i+M_n+H]^+)/(([M_i+H]^+ + [M_n+H]^+)*p^{ext}_{in}))$ **(D-F)** Fractional dimer compositions as computed after setting the $[Gly+Asp+H]^+$ peak intensity to zero.

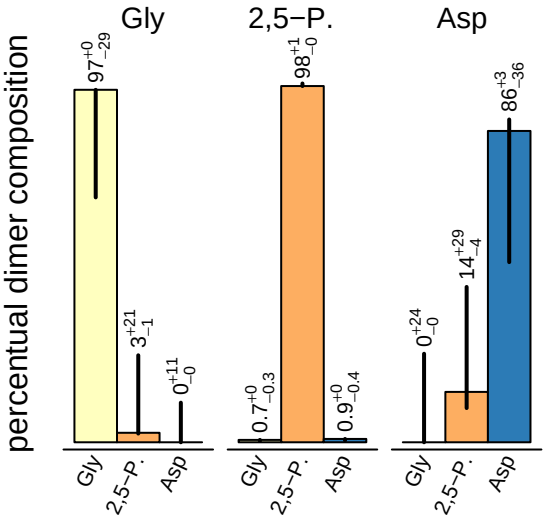

Figure 3.6: **Molecular interactions in a thin film containing glycine, 2,5-piperazinedione and asparagine.** Relative probabilities to form a non-covalent pair with a specific pairing partner for each of the molecules in a drop-deposited film consisting of glycine (Gly), asparagine (Asp) and 2,5-piperazinedione (2,5-P.) in the molar ratio 1:1:1. The values plotted are computed through normalization of the $[M_i+M_j+H]^+$ counts to the ionization potential of its constituting molecules as obtained from the $[M_{i,j}]^+$ counts. The error bars indicate the range of values obtained based on the different assumptions made as shown in Table 3.2. The transmission and detection probabilities are assumed equal for all pairings as each interacts with the other through hydrogen bonding and the molecules are of similar masses on the scale at which a loss of detection probability would be expected[95].

3.6 Summary

The $[nM+H]^+$ peaks assigned to supramolecular assemblies which are observed in all proteinogenic amino acids, a number of monosaccharides, and selected molecules not interacting though hydrogen bonding, are an indication that the extraction of supramolecular secondary ions is not an exception but a common phenomenon. Supramolecular assemblies and strongly fragmented species are observed within the same spectra. A possible explanation for this coexistence is that the supramolecular secondary ions detected desorb further away from the primary ion impact location than the routinely studied fragment secondary ions. In contrast to early studies conducted using heavy mono-atomic primary ions[88], it is observed here that the peak intensities attributed to potential chemical reaction products among the secondary ions remain several orders of magnitude below those of intact supramolecular clusters extracted as such from the bulk.

The observation, that supramolecular assemblies and networks are commonly preserved throughout the processes of desorption and ionization, paves the way to use SIMS as a tool in the study of molecular interactions and short-range supramolecular ordering in non-crystalline organic matter. Mass spectrometry is already successfully used in the identification of the structure of complex branched organic macromolecules[96], and analogue procedures for the analysis of supramolecular structuring in organic matter could be used. Similarly, in the screening for, and quantification of, non-covalent interactions in organic and biological solid and soft matter, procedures that have been developed for ESI[82,84] could be adapted.

Materials and Methods

Silicon substrate preparation. 1x1 cm^2 silicon wafers were cleaned in three steps in an ultrasound bath over a duration of 2x15 min in Acetone and 1x15 min in ethanol and subsequently exposed to oxygen plasma over a duration of 10 min.
Sample preparation. Sample molecules were purchased in high purity from Sigma Aldrich, Dextran (T5, 5'200 u, polydispersity 1.8) from Pharma-cosmos A/S, Denmark. The molecules were separately dissolved in pure H_2O (Sigma-

34877) at a concentration of 3 μg/ml and agitated using a vortex mixer to prepare pure stock solutions. Out of these stock solutions, sample solutions were prepared by pipetting to achieve the mass ratios indicated in the manuscript and again agitated using a vortex mixer. 50 μl of each sample was drop-deposited on a separate plasma-treated silicon wafer of 1x1 cm^2. It was assured that the deposited droplet spread over the entire available Si wafer surface, which had been rendered hydrophilic by the plasma treatment minutes prior to drop deposition. The samples were left to dry in a laminar flow chamber and analyzed the same day by ToF-SIMS.

ToF-SIMS data acquisition. Secondary ion mass spectrometry measurements were conducted on a ToF-SIMS.5 from IONTOF GmbH, Germany. The instrument was operated in spectroscopy mode and Bi_3^+ primary ions were used to analyze an area of 100x100 μm^2. The extractor voltage used was 3000 V, providing increased sensitivity in the high mass range.

Quantum chemistry simulations. All quantum chemistry calculations were performed using the GAMESS-US package[97] using the 6-311(2d,p) basis sets for all elements. The geometries were fully optimized up to a force threshold of 10-4 a.u. and the binding energy computed including the basis set superposition error correction using the procedure by Boys and Bernardi[98]. All calculations were conducted with several exchange-correlation functionals of the meta-GGA family ([90] and references therein), finding minimal differences in the binding energies. The reported binding energies and configurations were obtained with the M11 functional, a range-separated hybrid functional with 42.8 % Hartree-Fock exchange in the short-range and 100 % in the long-range. The figures including the molecular electrostatic potential coloring of the density isosurface (Fig. 1C) are realized with the software UCSF Chimera[99] interfaced with the package MacMolPlt[100].

3.7 Suggested improvements for supramolecular secondary ion mass spectrometry

Currently available secondary ion mass spectrometers are not optimized for the analysis of supramolecular secondary ions. In the following, adaptations of the

ionization process and of the detector technology are discussed which would improve the performance of a hypothetical instrument dedicated to the analysis of secondary ions and/or secondary neutrals.

Detectors: In standard commercial ToF-SIMS analyzers, microchannel plate detectors[101] are employed. The detection sensitivity of microchannel plates decreases strongly with increasing mass of the impacting molecule[102,95]. In the analysis of supramolecular structures by means of ToF-SIMS, the signal-to-noise ratio of high-mass peaks is observed to currently be one of the liming factors, besides the stability of supramolecular secondary ions. This limiting factor can be overcome by learning from the mass spectrometric techniques MALDI and ESI, which more routinely are used for the analysis of ions in the range between 1000 u and 1'000'000 u[103,104]. Dedicated cryo-detectors developed for this application[105,106] are more expensive in operation than microchannel plates due to typical operation temperatures below 4 K[103], but show a mass-independent detection efficiency close to 100 %[107,108]. The use of cryogenic detectors successfully allows ions in the mass range of 1'000'000 u to be studied[103,104]. Also the accurate detection of supramolecular ions is demonstrated for cryogenic detectors[104].

Primary ion sources: In the present work, Bi_3^+ primary ions are used. The extraction of supramolecular clusters consisting of small bio-molecules such as amino acids and monosaccharides is demonstrated. Compared to Bi_3^+, argon cluster primary ions are known to allow the extraction of larger unfragmented molecules. Using argon cluster primary ions, the extraction of intact bio-molecules up to a mass of 25'000 u has been demonstrated[109]. Correspondingly, it can be expected, that argon gas cluster primary ions would also allow the study of larger supramolecular clusters, as well as supramolecular clusters consisting of larger molecules. (Sidenote, the lateral resolution currently obtainable for argon cluster ion beams is around 10 µm[110], thus ca. 2 orders of magnitude lower than the resolution for bismuth guns.)

Post-ionization: Among the molecules, molecular fragments, and clusters ejected following a primary ion impact, less than 1 % possess charge and are sec-

ondary ions. Laser post-ionization allows the signal yield to be increased through targeting the ejected species that do not possess charge (see SNMS[21]). First trials combining argon cluster primary ion guns and laser post-ionization have been conducted on organic molecules of ca. 500 u mass and show an intensity increase for the unfragmented molecule of a factor of 10 compared to laser-post-ionization of molecules sputtered with Bi_3^+.[21] For supramolecular clusters desorbed from the surface, selective frequency tuning during laser post-ionization further holds the promise to yield spectra that reveal all clusters that contain a specific molecule of interest. Such selective laser post-ionization of supramolecular clusters can be expected to allow to fully quantitatively determine the statistical surroundings of any given molecule in a chemically complex system by removing the uncertainty resulting from cluster composition-dependent ionization probabilities from the equation.

4 Summary and Outlook

Secondary ion mass spectrometry is an analytical technique commonly used to qualitatively map spacial molecular concentration distributions with sub-micrometer resolution. In this thesis, it is shown that SIMS can also resolve the time-dependence of molecular concentration distributions across operating thin film electronic devices and from this assess the evolution of chemical equilibria. The time-dependence of molecular concentration distributions and local chemical equilibria across operating thin film electronic devices is studied in light-emitting electrochemical cells which are used as model system. LECs are operated *in-situ*, in the ToF-SIMS instrument, and are cooled down after well-defined operation times to freeze dynamic processes at the time-points of interest. Series of measurements on different electrodes of the same device are conducted to capture the internal device chemistry at different time points after voltage application. Sequences of discrete measurements conducted at different time points after voltage is applied to the LEC can be used to determine the time-dependence of the continuous processes that occur within the device. In particular, the voltage-induced reorganization of the density distribution of molecular ions that are dissolved in the organic layer of the LEC device is resolved. It is observed that this voltage-induced reorganization of the ionic density distribution locally shifts the chemical equilibria governing the number of free molecular ions, thus molecular ions whose charge is not directly compensated, such that the total number of free ions increases. Further, sequences of measurements conducted at different time points after voltage application resolve the formation of the electric double layer at the electrode interface when the devices are capped with a silver electrode, and show that aluminium electrodes progressively corrode in the same setting.

A further major achievement is the demonstration that intact supramolecular

assemblies of weakly bound molecules can be detected by SIMS. The conditions under which supramolecular secondary ions can be detected are studied on drop deposited films consisting of organic molecules, which are selected based on their ability to interact with each other via weak forces such as hydrogen bonds or pi-interactions. ToF-SIMS mass spectra acquired on films consisting of a single molecular species are observed to, in the majority of cases studied, contain series of peaks at masses corresponding to charged supramolecular assemblies of the type $[nM\pm H]^{\pm}$, where n is an integer larger than 1, M the molecular mass of the molecule deposited and H the mass of hydrogen. Peaks attributed to such supramolecular secondary ions are observed to vanish from the mass spectrum with increasing ion impact damage. From this observation it must be concluded that the detected supramolecular assemblies were not formed by the primary ion impact but must have existed on the surface of the sample.

In a first series of experiments, drop deposited films, each containing a single molecular species, were fabricated for all 21 proteinogenic amino acids and for a set of 19 monosaccharides. Amino acids and monosaccharides are known to interact through hydrogen bonding. The mass spectra of all proteinogenic amino acids and all monosaccharides studied showed peaks corresponding to supramolecular secondary ions. The relative intensities of the $[nM\pm H]^{\pm}$ peaks within a spectrum are observed to vary for different molecules. Among the most remarkable observations made, is that within the series of $[nM\pm H]^{\pm}$ peaks in the spectrum of a molecule, specific $[nM\pm H]^{\pm}$ peaks can have a higher intensity than nearby supramolecular peaks of lower mass. The pattern of $[nM\pm H]^{\pm}$ peaks within a spectrum can allow conclusions on the molecular arrangement on the surface of the sample. The example discussed in detail in this thesis is that of the amino acid proline, which is inferred to form closed assemblies of 12 molecules upon drying. This is in contrast to previous XRD work that finds proline to assemble in crystallites. From this we conclude that both types of supramolecular assemblies can co-exist in solid proline.

In a second series of experiments, films that each consisted of a set of either 2, 3, or 4 different, selected, molecules were used as model systems. In mass spectra acquired on these films, supramolecular clusters consisting of molecules of different

types are observed. The probability of two different molecules to be found in the same supramolecular cluster is related to the probability of these two molecules being direct neighbors on the surface probed. It is demonstrated that conclusions on the statistics of molecular surroundings can be made from an analysis of the peaks corresponding to supramolecular dimers of different molecular pairings.

In a dynamic system, such as a biological cell, the analysis of supramolecular dimers contained in a spectrum would translate into the resolution of relative molecular interaction probabilities. Note however, that for the study of molecular interaction probabilities in complex biological systems by means of ToF-SIMS, several difficulties need to be overcome. Firstly, in order to preserve the molecular arrangements, the biological sample needs to be vitrified and sectioned in its vitrified state. The cross-sections need to be subsequently transferred into the instrument and analysed while maintaining a temperature that is sufficiently low as to not allow for ice crystal formation within the cross-section. In the transfer process, deposition of atmospheric water on the cold surface of the vitrified cross-sections has to be prevented because ToF-SIMS as an analytical technique is only sensitive to the very few molecular surface layers. Secondly, the identification of supramolecular peaks in spectra acquired on complex biological systems has yet to be demonstrated in a proof of concept study. To approach this goal, the extraction of supramolecular assemblies from well defined, drop-cast, amorphous systems containing multiple different molecules is demonstrated within this thesis.

Bibliography

[1] J. C. Vickermann and D. Briggs. *ToF-SIMS: Materials Analysis by Mass Spectrometry*. IM Publications LLP and SurfaceSpectra Limited, Manchester, 2nd edition, 2013.

[2] B A Mamyrin, V I Karataev, D V Shmikk, and V A Zagulin. The mass-reflectron, a new nonmagnetic time-of-flight mass spectrometer with high resolution. *Zh. Eksp. Teor. Fiz.*, 64:45–48, 1973.

[3] Qizhi Hu, Robert J. Noll, Hongyan Li, Alexander Makarov, Mark Hardman, and R. Graham Cooks. The Orbitrap: a new mass spectrometer. *Journal of Mass Spectrometry*, 40(4):430–443, 2005.

[4] Sergey V. Baryshev, Alexander V. Zinovev, C. Emil Tripa, Michael J. Pellin, Qing Peng, Jeffrey W. Elam, and Igor V. Veryovkin. High-resolution secondary ion mass spectrometry depth profiling of nanolayers: Depth profiling of nanolayers by high-resolution SIMS. *Rapid Communications in Mass Spectrometry*, 26(19):2224–2230, 2012.

[5] Celine Noel, Yan Busby, Nicolas Mine, and Laurent Houssiau. ToF-SIMS Depth Profiling of Organic Delta Layers with Low-Energy Cesium Ions: Depth Resolution Assessment. *Journal of The American Society for Mass Spectrometry*, 30(8):1537–1544, 2019.

[6] Kyung Joong Kim, David Simons, and Greg Gillen. Quantitative depth profiling of an alternating Pt/Co multilayer and a Pt–Co alloy multilayer by SIMS using a Buckminsterfullerene (C60) source. *Applied Surface Science*, 253(14):6000–6005, 2007.

[7] M.P. Seah and A.G. Shard. The matrix effect in secondary ion mass spectrometry. *Applied Surface Science*, 439:605–611, 2018.

[8] Elena S. F. Berman, Kristen S. Kulp, Mark G. Knize, Ligang Wu, Erik J. Nelson, David O. Nelson, and Kuang Jen Wu. Distinguishing Monosaccharide Stereo- and Structural Isomers with TOF-SIMS and Multivariate Statistical Analysis. *Analytical Chemistry*, 78(18):6497–6503, 2006.

[9] Sabine Holzer, Stefan Krivec, Sven Kayser, Julia Zakel, and Herbert Hutter. Large O2 Cluster Ions as Sputter Beam for ToF-SIMS Depth Profiling of Alkali Metals in Thin SiO2 Films. *Analytical Chemistry*, 89(4):2377–2382, 2017.

[10] M. Kawecki, R. Hany, M. Diethelm, S. Jenatsch, Q. Grossmann, L. Bernard, and H. J. Hug. Direct Measurement of Ion Redistribution and Resulting-Modification of Chemical Equilibria in Polymer Thin Film Light-Emitting Electrochemical Cells. *Appl. Mater. Interf.*, 10:39100, 2018.

[11] F Kollmer. Cluster primary ion bombardment of organic materials. *Applied Surface Science*, 231-232:153–158, 2004.

[12] D. Touboul, F. Kollmer, E. Niehuis, A. Brunelle, and O. Laprevote. Improvment of biological time-of-flight secondary ion mass spectrometry imaging with a bismuth cluster ion source. *Am. Soc. Mass Spectrom*, 16:1608–1618, 2005.

[13] R J Colton. Molecular secondary ion mass spectrometry (SIMS). *J. Vac. Sci. Technol.*, 18:737–747, 1981.

[14] Felix Kollmer, Wolfgang Paul, Martin Krehl, and Ewald Niehuis. Ultra high spatial resolution SIMS with cluster ions - approaching the physical limits: Ultra high spatial resolution SIMS. *Surface and Interface Analysis*, 45(1):312–314, 2013.

[15] I. T. Joliffe. *Principal component analysis*. Springer, New York, 2 edition, 2002.

[16] Mark C. Biesinger, Pierre-Yves Paepegaey, N. Stewart McIntyre, Robert R. Harbottle, and Nils O. Petersen. Principal Component Analysis of TOF-SIMS Images of Organic Monolayers. *Analytical Chemistry*, 74(22):5711–5716, 2002.

[17] Daniel J. Graham and David G. Castner. Multivariate Analysis of ToF-SIMS Data from Multicomponent Systems: The Why, When, and How. *Biointerphases*, 7(1):49, 2012.

[18] X Vanden Eynde and P Bertrand. ToF-SIMS Quantifcation of Polystyrene Spectra based on Principal Component Analysis (PCA). *Surface and Interface Analysis*, 25:878–888, 1997.

[19] I Yamada. Materials processing by gas cluster ion beams. *Materials Science and Engineering: R: Reports*, 34(6):231–295, 2001.

[20] Kan Shen, Andreas Wucher, and Nicholas Winograd. Molecular Depth Profiling with Argon Gas Cluster Ion Beams. *The Journal of Physical Chemistry C*, 119(27):15316–15324, 2015.

[21] Marcel Heeger, Bonnie J. Tyler, Martin Körsgen, and Heinrich F. Arlinghaus. Laser postionization of neutral molecules sputtered using bismuth and argon cluster primary ions. *Biointerphases*, 13(3):03B412, 2018.

[22] Winfried Denk and Heinz Horstmann. Serial Block-Face Scanning Electron Microscopy to Reconstruct Three-Dimensional Tissue Nanostructure. *PLoS Biology*, 2(11):e329, 2004.

[23] Wolfgang Brütting, Jorg Frischeisen, Tobias D. Schmidt, Bert J. Scholz, and Christian Mayr. Device efficiency of organic light-emitting diodes: Progress by improved light outcoupling. *Physica Status Solidi A*, 210(1):44–65, 2013.

[24] Zhengqi Shi and Ahalapitiya Jayatissa. Perovskites-Based Solar Cells: A Review of Recent Progress, Materials and Processing Methods. *Materials*, 11(5):729, 2018.

[25] Yong Cui, Huifeng Yao, Jianqi Zhang, Tao Zhang, Yuming Wang, Ling Hong, Kaihu Xian, Bowei Xu, Shaoqing Zhang, Jing Peng, Zhixiang Wei, Feng Gao, and Jianhui Hou. Over 16% efficiency organic photovoltaic cells enabled by a chlorinated acceptor with increased open-circuit voltages. *Nature Communications*, 10(1):2515, 2019.

[26] Seung-Min Lim, Hyunjae Yoo, Min-Ah Oh, Seok Hee Han, Hae-Ryung Lee, Taek Dong Chung, Young-Chang Joo, and Jeong-Yun Sun. Ion-to-ion amplification through an open-junction ionic diode. *Proceedings of the National Academy of Sciences*, 116(28):13807–13815, 2019.

[27] Krzysztof Fic, Anetta Platek, Justyna Piwek, and Elzbieta Frackowiak. Sustainable materials for electrochemical capacitors. *Materials Today*, 21(4):437–454, 2018.

[28] F. Fu, S. Pisoni, Q. Jeangros, J. Sastre-Pelicer, M. Kawecki, A. Paracchino, T. Moser, J. Werner, C. Andres, L. Duchene, P. Fiala, M. Rawlence, S. Nicolay, C. Ballif, A. N. Tiwari, and S. Buecheler. I2 vapor-induced degradation of formamidinium lead iodide based perovskite solar cells under heat-light soaking conditions. *Energy & Environmental Science*, 12:3074–3088, 2019.

[29] Kui Zhao, Olga Wodo, Dingding Ren, Hadayat Ullah Khan, Muhammad Rizwan Niazi, Hanlin Hu, Maged Abdelsamie, Ruipeng Li, Er. Qiang Li, Liyang Yu, Buyi Yan, Marcia M. Payne, Jeremy Smith, John E. Anthony, Thomas D. Anthopoulos, Sigurdur T. Thoroddsen, Baskar Ganapathysubramanian, and Aram Amassian. Vertical Phase Separation in Small Molecule:Polymer Blend Organic Thin Film Transistors Can Be Dynamically Controlled. *Advanced Functional Materials*, 26(11):1737–1746, 2016.

[30] M. Diethelm, Q. Grossmann, A. Schiller, E. Knapp, S. Jenatsch, M. Kawecki, F. Nuesch, and R. Hany. Optimized Electrolyte Loading and Active Film Thickness for Sandwich Polymer Light-Emitting Electrochemical Cells. *Adv. Opt. Mater.*, 7:1801278, 2019.

[31] M. Diethelm, A. Schiller, M. Kawecki, A. Devizis, B. Blulle, S. Jenatsch, E. Knapp, Q. Grossmann, B. Ruhstaller, F. Nuesch, and R. Hany. The Dy-

namic Emission Zone in Sandwich Polymer Light-Emitting Electrochemical Cells. *Adv. Mater.*, in print, 2019.

[32] W. Xu, Q. Hu, S. Bai, C. Bao, Y. Miao, Z. Yuan, T. Borzda, A. J. Barker, E. Tyukalova, Z. Hu, M. Kawecki, H. Wang, Z. Yan, X. Liu, X. Shi, K. Uvdal, M. Fahlman, W. Zhang, M. Duchamp, J.-M. Liu, A. Petrozza, J. Wang, L.-M. Liu, W. Huang, and F. Gao. Rational molecular passivation for high-performance perovskite light-emitting diodes. *Nature Photonics*, 13:418–424, 2019.

[33] S. Bai, P. Da, C. Li, Z. Wang, Z. Yuan, F. Fu, M. Kawecki, X. Liu, N. Sakai, J. T.-W. Wang, S. Huettner, S. Buecheler, M. Fahlman, F. Gao, and H. J. Snaith. Planar perovskite solar cells with long-term stability using ionic liquid additives. *Nature*, 571:245–250, 2019.

[34] M. J. I. Airaghi Leccardi, N. A. L. Chenais, L. Ferlauto, M. Kawecki, E. G. Zolliger, and D. Ghezzi. Tailored polymeric, photovoltaic, and near-infrared-responsive neuroprosthesis. *Nat. Commun.*, submitted.

[35] Ruben D. Costa, editor. *Light-emitting electrochemical cells*. Springer Berlin Heidelberg, New York, NY, 2017.

[36] Sebastian B. Meier, Daniel Tordera, Antonio Pertegas, Cristina Roldán-Carmona, Enrique Orti, and Henk J. Bolink. Light-emitting electrochemical cells: recent progress and future prospects. *Materials Today*, 17(5):217–223, 2014.

[37] Qibing Pei, Gang Yu, Chi Zhang, Yang Yang, and Alan J Heeger. Polymer Light-Emitting Electrochemical Cells. *Science*, 269:4, 1995.

[38] Shi Tang, Andreas Sandstrom, Petter Lundberg, Thomas Lanz, Christian Larsen, Stephan van Reenen, Martijn Kemerink, and Ludvig Edman. Design rules for light-emitting electrochemical cells delivering bright luminance at 27.5 percent external quantum efficiency. *Nature Communications*, 8(1):1190, 2017.

[39] J. C. deMello, N. Tessler, S. C. Graham, and R. H. Friend. Ionic space-charge effects in polymer light-emitting diodes. *Physical Review B*, 57(20):12951–12963, 1998.

[40] J. C. deMello. Interfacial feedback dynamics in polymer light-emitting electrochemical cells. *Physical Review B*, 66(23):235210, 2002.

[41] Qibing Pei, Yang Yang, Gang Yu, Chi Zhang, and Alan J. Heeger. Polymer Light-Emitting Electrochemical Cells: In Situ Formation of a Light-Emitting p-n Junction. *Journal of the American Chemical Society*, 118(16):3922–3929, 1996.

[42] David J. Dick, Alan J. Heeger, Yang Yang, and Qibing Pei. Imaging the structure of the p-n junction in polymer light-emitting electrochemical cells. *Advanced Materials*, 8(12):985–987, 1996.

[43] Ludvig Edman. Bringing light to solid-state electrolytes: The polymer light-emitting electrochemical cell. *Electrochimica Acta*, 50(19):3878–3885, 2005.

[44] Nathaniel D. Robinson, Joon-Ho Shin, Magnus Berggren, and Ludvig Edman. Doping front propagation in light-emitting electrochemical cells. *Physical Review B*, 74(15):155210, 2006.

[45] Jason D. Slinker, John A. DeFranco, Michael J. Jaquith, William R. Silveira, Yu-Wu Zhong, Jose M. Moran-Mirabal, Harold G. Craighead, Hector D. Abruna, John A. Marohn, and George G. Malliaras. Direct measurement of the electric-field distribution in a light-emitting electrochemical cell. *Nature Materials*, 6(11):894–899, 2007.

[46] Qibing Pei and Alan J. Heeger. Operating mechanism of light-emitting electrochemical cells. *Nature Materials*, 7:167, 2008.

[47] Piotr Matyba, Klara Maturova, Martijn Kemerink, Nathaniel D. Robinson, and Ludvig Edman. The dynamic organic p–n junction. *Nature Materials*, 8(8):672–676, 2009.

[48] Stephan van Reenen, Piotr Matyba, Andrzej Dzwilewski, Rene A. J. Janssen, Ludvig Edman, and Martijn Kemerink. A Unifying Model for the Operation of Light-Emitting Electrochemical Cells. *Journal of the American Chemical Society*, 132(39):13776–13781, 2010.

[49] Samuel B. Toshner, Zihua Zhu, Ilya V. Kosilkin, and Janelle M. Leger. Characterization of Ion Profiles in Light-Emitting Electrochemical Cells by Secondary Ion Mass Spectrometry. *ACS Applied Materials & Interfaces*, 4(3):1149–1153, 2012.

[50] Tyko D. Shoji, Zihua Zhu, and Janelle M. Leger. Characterizing Ion Profiles in Dynamic Junction Light-Emitting Electrochemical Cells. *ACS Applied Materials & Interfaces*, 5(22):11509–11514, 2013.

[51] Shi Tang and Ludvig Edman. Quest for an Appropriate Electrolyte for High-Performance Light-Emitting Electrochemical Cells. *The Journal of Physical Chemistry Letters*, 1(18):2727–2732, 2010.

[52] Shi Tang, Jonas Mindemark, Carlos Moyses Graca Araujo, Daniel Brandell, and Ludvig Edman. Identifying Key Properties of Electrolytes for Light-Emitting Electrochemical Cells. *Chemistry of Materials*, 26(17):5083–5088, 2014.

[53] Sandra Jenatsch, Lei Wang, Matia Bulloni, Anna C. Véron, Beat Ruhstaller, Stephane Altazin, Frank Nuesch, and Roland Hany. Doping Evolution and Junction Formation in Stacked Cyanine Dye Light-Emitting Electrochemical Cells. *ACS Applied Materials & Interfaces*, 8(10):6554–6562, 2016.

[54] Jonas Mindemark, Shi Tang, Jia Wang, Nikolai Kaihovirta, Daniel Brandell, and Ludvig Edman. High-Performance Light-Emitting Electrochemical Cells by Electrolyte Design. *Chemistry of Materials*, 28(8):2618–2623, 2016.

[55] Takahiro Ohe, Miki Kuribayashi, Ryoichi Yasuda, Ami Tsuboi, Kazumasa Nomoto, Kotaro Satori, Masao Itabashi, and Jiro Kasahara. Solution-processed organic thin-film transistors with vertical nanophase separation. *Applied Physics Letters*, 93(5):053303, 2008.

[56] Cecilia M. Bjorstrom, Svante Nilsson, Andrzej Bernasik, Andrzej Budkowski, Mats Andersson, Kjell O. Magnusson, and Ellen Moons. Vertical phase separation in spin-coated films of a low bandgap polyfluorene/PCBM blend—Effects of specific substrate interaction. *Applied Surface Science*, 253(8):3906–3912, 2007.

[57] Y. Shao, G. C. Bazan, and A. J. Heeger. Long-Lifetime Polymer Light-Emitting Electrochemical Cells. *Advanced Materials*, 19(3):365–370, 2007.

[58] Jakob Heier, Jan Groenewold, Simon Huber, Frank Nüesch, and Roland Hany. Nanoscale Structuring of Semiconducting Molecular Blend Films in the Presence of Mobile Counterions. *Langmuir*, 24(14):7316–7322, 2008.

[59] F. P. Wenzl, P. Pachler, C. Suess, A. Haase, E. J. W. List, P. Poelt, D. Somitsch, P. Knoll, U. Scherf, and G. Leising. The Influence of the Phase Morphology on the Optoelectronic Properties of Light-Emitting Electrochemical Cells. *Advanced Functional Materials*, 14(5):441–450, 2004.

[60] Stephan van Reenen, Rene A. J. Janssen, and Martijn Kemerink. Fundamental Tradeoff between Emission Intensity and Efficiency in Light-Emitting Electrochemical Cells. *Advanced Functional Materials*, 25(20):3066–3073, May 2015.

[61] D. L. Smith. Steady state model for polymer light-emitting electrochemical cells. *Journal of Applied Physics*, 81(6):2869–2880, March 1997.

[62] Joon Ho Shin, Piotr Matyba, Nathaniel D. Robinson, and Ludvig Edman. The influence of electrodes on the performance of light-emitting electrochemical cells. *Electrochimica Acta*, 52(23):6456–6462, 2007.

[63] Kang Xu. Nonaqueous Liquid Electrolytes for Lithium-Based Rechargeable Batteries. *Chemical Reviews*, 104(10):4303–4418, 2004.

[64] E. Mattias Lindh, Petter Lundberg, Thomas Lanz, Jonas Mindemark, and Ludvig Edman. The Weak Microcavity as an Enabler for Bright and Fault-tolerant Light-emitting Electrochemical Cells. *Scientific Reports*, 8(1):6970, 2018.

[65] J. E. Heuser. Synaptic vesicle exocytosis captured by quick freezing and correlated with quantal transmitter release. *The Journal of Cell Biology*, 81(2):275–300, 1979.

[66] Sven Ruhle. Tabulated values of the Shockley–Queisser limit for single junction solar cells. *Solar Energy*, 130:139–147, 2016.

[67] https://www.nrel.gov/pv/assets/pdfs/best-research-cell-efficiencies.pdf, November 2019.

[68] Zhaoning Song, Cong Chen, Chongwen Li, Rasha A Awni, Dewei Zhao, and Yanfa Yan. Wide-bandgap, low-bandgap, and tandem perovskite solar cells. *Semiconductor Science and Technology*, 34(9):093001, 2019.

[69] Se-Yun Kim, Yeonghun Yun, Seunghak Shin, Joon Hyung Lee, Young-Woo Heo, and Sangwook Lee. Wide range tuning of band gap energy of A3b2x9 perovskite-like halides. *Scripta Materialia*, 166:107–111, 2019.

[70] Stefan A. L. Weber, Ilka M. Hermes, Silver-Hamill Turren-Cruz, Christopher Gort, Victor W. Bergmann, Laurent Gilson, Anders Hagfeldt, Michael Graetzel, Wolfgang Tress, and Rüdiger Berger. How the formation of interfacial charge causes hysteresis in perovskite solar cells. *Energy & Environmental Science*, 11(9):2404–2413, 2018.

[71] Fangfang Wang, Yezhou Cao, Cheng Chen, Qing Chen, Xiao Wu, Xinguo Li, Tianshi Qin, and Wei Huang. Materials toward the Upscaling of Perovskite Solar Cells: Progress, Challenges, and Strategies. *Advanced Functional Materials*, 28(52):1803753, 2018.

[72] A.S. Bhalla, Ruyan Guo, and Rustum Roy. The perovskite structure—a review of its role in ceramic science and technology. *Materials Research Innovations*, 4(1):3–26, 2000.

[73] S. D. Stranks, G. E. Eperon, G. Grancini, C. Menelaou, M. J. P. Alcocer, T. Leijtens, L. M. Herz, A. Petrozza, and H. J. Snaith. Electron-Hole Diffusion Lengths Exceeding 1 Micrometer in an Organometal Trihalide Perovskite Absorber. *Science*, 342(6156):341–344, 2013.

[74] Martin Kaltenbrunner, Getachew Adam, Eric Daniel Głowacki, Michael Drack, Reinhard Schwödiauer, Lucia Leonat, Dogukan Hazar Apaydin, Heiko Groiss, Markus Clark Scharber, Matthew Schuette White, Niyazi Serdar Sariciftci, and Siegfried Bauer. Flexible high power-per-weight perovskite solar cells with chromium oxide–metal contacts for improved stability in air. *Nature Materials*, 14(10):1032–1039, 2015.

[75] Antonio Guerrero, Jingbi You, Clara Aranda, Yong Soo Kang, Germà Garcia-Belmonte, Huanping Zhou, Juan Bisquert, and Yang Yang. Interfacial Degradation of Planar Lead Halide Perovskite Solar Cells. *ACS Nano*, 10(1):218–224, 2016.

[76] Christopher Sutton, Chad Risko, and Jean-Luc Brédas. Noncovalent Intermolecular Interactions in Organic Electronic Materials: Implications for the Molecular Packing vs Electronic Properties of Acenes. *Chemistry of Materials*, 28(1):3–16, 2016.

[77] Riccardo Baron and J. Andrew McCammon. Molecular Recognition and Ligand Association. *Annual Review of Physical Chemistry*, 64(1):151–175, 2013.

[78] Christopher M Dobson. Protein folding and misfolding. *Nature*, 426:884–890, 2003.

[79] M Baldus. Molecular interactions investigated by multi-dimensional solid-state NMR. *Current Opinion in Structural Biology*, 16(5):618–623, 2006.

[80] Parthapratim Munshi and Tayur N. Guru Row. Evaluation of weak intermolecular interactions in molecular crystals *via* experimental and theoretical charge densities. *Crystallography Reviews*, 11(3):199–241, 2005.

[81] Z. Hong Zhou. Atomic resolution cryo electron microscopy of macromolecular complexes. In *Advances in Protein Chemistry and Structural Biology*, volume 82, pages 1–35. Elsevier, 2011.

[82] Sonya M. Clark and Lars Konermann. Screening for Noncovalent Ligand-Receptor Interactions by Electrospray Ionization Mass Spectrometry-Based Diffusion Measurements. *Analytical Chemistry*, 76(5):1257–1263, 2004.

[83] J. A. Loo. Studying noncovalent protein complexes by electrospray ionization mass spectrometry. *Mass Spectrom. Rev.*, 16:1–23, 1997.

[84] Elisabetta Boeri Erba, Konstantin Barylyuk, Yang Yang, and Renato Zenobi. Quantifying Protein–Protein Interactions Within Noncovalent Complexes Using Electrospray Ionization Mass Spectrometry. *Analytical Chemistry*, 83(24):9251–9259, 2011.

[85] Dror S. Chorev, Lindsay A. Baker, Di Wu, Victoria Beilsten-Edmands, Sarah L. Rouse, Tzviya Zeev-Ben-Mordehai, Chimari Jiko, Firdaus Samsudin, Christoph Gerle, Syma Khalid, Alastair G. Stewart, Stephen J. Matthews, Kay Grünewald, and Carol V. Robinson. Protein assemblies ejected directly from native membranes yield complexes for mass spectrometry. *Science*, 362(6416):829–834, 2018.

[86] S. Madler, E. B. Erba, and R. Zenobi. MALDI-ToF mass spectrometry for studying non-covalent complexes of biomolecules. In *Applications of MALDI-ToF Spectrometry*, pages 1–36. Springer, Heidelberg, 2013.

[87] H. T. Jonkman and J. Michl. Secondary Ion Mass Spectrometry of small molecules held at cryogenic temperatures. In *Secondary Ion Mass Spectrometry SIMS II*, pages 292–295. Springer, Berlin, 1979.

[88] R. G. Orth, H. T. Jonkman, and J. Michl. Secondary ion mass spectrometry of molecular solids, a source of cluster ions. *J. Am. Chem. Soc.*, 103:1564–1565, 1981.

[89] S. Myung, K. P. Lorton, S. I. Merenbloom, M. Fioroni, S. L. Koeniger, R. R. Julian, M.-H. Baik, and D. E. Clemmer. Evidence for spontaneous resolution of icosahedral proline. *J. Am. Chem. Soc.*, 128:15988–15989, 2006.

[90] Roberto Peverati and Donald G. Truhlar. Improving the Accuracy of Hybrid Meta-GGA Density Functionals by Range Separation. *The Journal of Physical Chemistry Letters*, 2(21):2810–2817, 2011.

[91] R. B. Corey. The crystal structure of diketopiperazine. *J. Am. Chem. Soc.*, 60:1598–1604, 1938.

[92] R. Degeilh and R. E. Marsh. A refinement of the crystal structure of diketopiperazine (2,5- piperazinedione). *Acta. Cryst.*, 12:1007–1014, 1959.

[93] J. Huddleston, A. Veide, K. Kohler, J. Flangan, S.-O. Enfors, and A. Lyddiatt. The molecular basis of partitioning in aqueous two-phase systems. *Trends Biotechnol.*, 9:381–388, 1991.

[94] K. Ratanapongleka. Recovery of biological products in aqueous two phase systems. *Int. J. Chem. Eng. Appl.*, 1.:191–198, 2010.

[95] R Liu, Q. Li, and L. M. Smith. Detection of large ions in time-of-flight mass spectrometry: effects of ion mass and acceleration voltage on microchannel plate detector response. *J. Am. Soc. Mass Spectrom.*, 25:1374–1383, 2014.

[96] A. S. Weiskopf, P. Vouros, and D. J. Harvey. Electrospray ionization-ion trap mass spectrometry for structural analysis of complex n-linked glycoprotein oligosaccharides. *Anal. Chem.*, 70:4441–4447, 1998.

[97] Michael W. Schmidt, Kim K. Baldridge, Jerry A. Boatz, Steven T. Elbert, Mark S. Gordon, Jan H. Jensen, Shiro Koseki, Nikita Matsunaga, Kiet A. Nguyen, Shujun Su, Theresa L. Windus, Michel Dupuis, and John A. Montgomery. General atomic and molecular electronic structure system. *Journal of Computational Chemistry*, 14(11):1347–1363, 1993.

[98] S.F. Boys and F. Bernardi. The calculation of small molecular interactions by the differences of separate total energies. Some procedures with reduced errors. *Molecular Physics*, 19(4):553–566, 1970.

[99] Eric F. Pettersen, Thomas D. Goddard, Conrad C. Huang, Gregory S. Couch, Daniel M. Greenblatt, Elaine C. Meng, and Thomas E. Ferrin. UCSF

Chimera - A visualization system for exploratory research and analysis. *Journal of Computational Chemistry*, 25(13):1605–1612, 2004.

[100] Brett M. Bode and Mark S. Gordon. Macmolplt: a graphical user interface for GAMESS. *Journal of Molecular Graphics and Modelling*, 16(3):133–138, 1998.

[101] J. L. Wiza. Microchannel plate detectors. *Nucl. Instrum. Methods*, 162:587–601, 1979.

[102] G. Westmacott, M. Frank, S. E. Labov, and W. H. Benner. Using a superconducting tunnel junction detector to measure the secondary electron emission efficiency for a microchannel plate detector bombarded by large molecular ions. *Rapid Communications in Mass Spectrometry*, 14:1854–1861, 2000.

[103] Ryan J. Wenzel, Urs Matter, Lothar Schultheis, and Renato Zenobi. Analysis of Megadalton Ions Using Cryodetection MALDI Time-of-Flight Mass Spectrometry. *Analytical Chemistry*, 77(14):4329–4337, 2005.

[104] Alexander A. Aksenov and Mark E. Bier. The analysis of polystyrene and polystyrene aggregates into the mega dalton mass range by cryodetection MALDI TOF MS. *Journal of the American Society for Mass Spectrometry*, 19(2):219–230, 2008.

[105] Matthias Frank, Simon E Labov, Garrett Westmacott, and W Henry Benner. Energy-sensitive cryogenic detectors for high-mass biomolecule mass spectrometry. *Mass Spectrometry Reviews*, 18:155–186, 1999.

[106] M. Ohkubo. Superconducting detectors for particles from atoms to proteins. *Physica C: Superconductivity*, 468(15-20):1987–1991, 2008.

[107] Damian Twerenbold, Jean-Luc Vuilleumier, Daniel Gerber, Almut Tadsen, Ben van den Brandt, and Patrick M. Gillevet. Detection of single macromolecules using a cryogenic particle detector coupled to a biopolymer mass spectrometer. *Applied Physics Letters*, 68(24):3503–3505, 1996.

[108] M. Ohkubo, Y. Shigeri, T. Kinumi, N. Saito, M. Ukibe, Y.E. Chen, A. Kushino, A. Kurokawa, H. Sato, and S. Ichimura. Fragmentation analysis by superconducting ion detectors in matrix-assisted laser desorption/ionization (MALDI). *Nuclear Instruments and Methods in Physics Research Section A: Accelerators, Spectrometers, Detectors and Associated Equipment*, 559(2):779–781, 2006.

[109] K. Mochiji. Enhancement of Intact- Ion Yield and Surface Sensitivity by Argon-cluster SIMS. *J. Anal. Bioanal. Techniques*, S2:001, 2011.

[110] H. Tian, L. J. Sparvero, A. A. Amoscato, A. Bloom, H. Bayir, V.E. Kagan, and N. Winograd. Gas cluster ion beam time-of-flight secondary ion mass spectrometry high-resolution imaging of cardiolipin speciation in the brain: identification of molecular losses after traumatic injury. *Anal. Chem.*, 89:4611–4619, 2017.

[111] Melissa K. Passarelli and Nicholas Winograd. Lipid imaging with time-of-flight secondary ion mass spectrometry (ToF-SIMS). *Biochimica et Biophysica Acta (BBA) - Molecular and Cell Biology of Lipids*, 1811(11):976–990, 2011.

[112] https://www.leicabiosystems.com/pathologyleaders/fixation-and-fixatives-2-factors-influencing-chemical-fixation-formaldehyde-and-glutaraldehyde/, January 2019.

[113] https://www.leica-microsystems.com/science-lab/brief-introduction-to-freeze-substitution/, January 2019.

[114] B. Payre, E. Gontier, A. Jarray, Y. Martinez, J.P. Laugier, A. Delalleau, B.M. Gaillard, I. Anselme, D. GoudounèChe, I. Fourquaux, M. Hemati, V. Gerbaud, M.B. Delisle, and C. Guilbeau-Frugier. A new HPF specimen carrier adapter for the use of high-pressure freezing with cryoscanning electron microscope: two applications: stearic acid organization in a hydroxypropyl methylcellulose matrix and mice myocardium. *Journal of Microscopy*, 271(3):255–265, 2018.

[115] Paul A. Sims and Jeff D. Hardin. Fluorescence-Integrated Transmission Electron Microscopy Images. In John Kuo, editor, *Electron Microscopy: Methods and Protocols*, Methods in Molecular Biology™, pages 291–308. Humana Press, Totowa, NJ, 2007.

[116] Errin Johnson, Elena Seiradake, E. Yvonne Jones, Ilan Davis, Kay Grünewald, and Rainer Kaufmann. Correlative in-resin super-resolution and electron microscopy using standard fluorescent proteins. *Scientific Reports*, 5(1):9583, 2015.

[117] https://www.emsdiasum.com/microscopy/technical/datasheet/14330b.aspx, January 2019.

[118] Huy Bang Nguyen, Truc Quynh Thai, Sei Saitoh, Bao Wu, Yurika Saitoh, Satoshi Shimo, Hiroshi Fujitani, Hirohide Otobe, and Nobuhiko Ohno. Conductive resins improve charging and resolution of acquired images in electron microscopic volume imaging. *Scientific Reports*, 6(1):23721, 2016.

[119] Marialuigia Raimondo, Liberata Guadagno, Luigi Vertuccio, Carlo Naddeo, Giuseppina Barra, Giovanni Spinelli, Patrizia Lamberti, Vincenzo Tucci, and Khalid Lafdi. Electrical conductivity of carbon nanofiber reinforced resins: Potentiality of Tunneling Atomic Force Microscopy (TUNA) technique. *Composites Part B: Engineering*, 143:148–160, 2018.

[120] https://ncmir.ucsd.edu/sbem-protocol, January 2019.

Supplementary information

SI1. ToF-SIMS reference spectra databases for biological building blocks

Existing reference spectra of organic molecules are scarce. To fill the major gaps, complete databases of reference spectra for the 21 proteinogenic amino acids and glycine [1,2] as well as for 19 common monosaccharides [3, 4] were conducted.

[1] M. Kawecki* and L. Bernard, *Database of proteinogenic amino acid reference spectra for Bismuth-cluster ToF-SIMS. I. Negative polarity.* Surf.Sci.Spectra **25**(1), 015001 (2018)

[2] M. Kawecki* and L. Bernard, *Database of proteinogenic amino acid reference spectra for Bismuth-cluster ToF-SIMS. II. Positive polarity.* Surf.Sci.Spectra **25**(1), 015002 (2018)

[3] L Bernard, R Crockett and M Kawecki*, *Monosaccharides: a ToF-SIMS reference spectra database - Part 1/2: negative polarity*, Surf.Sci.Spectra **26**(2), in print

[4] L Bernard, R Crockett and M Kawecki*, *Monosaccharides: a ToF-SIMS reference spectra database - Part 2/2: negative polarity.*, Surf.Sci.Spectra **26**(2), in print

A satisfactory study containing reference peeks for lipids can already be found in literature[111].

SI2. Protocol for Si-wafer preparation for reference spectra

The protocol below aims at maximally reducing residual contaminations visible in the spectra while allowing for high throughput in a laboratory environment. It is developed for the preparation of freshly cut 1x1 cm2 silicon wafers to be used in standardized reference spectra.

1) 15 min ulstrasound bath treatment in acetone
aim: remove any major contaminations

2) 15 min ulstrasound bath treatment in ethanol
aim: remove residual contaminations with insufficient solubility in acetone

3) 15 min ulstrasound bath treatment in freshly de-ionized water (Resistivity $>$ 18.2 MΩ cm)
aim: remove sodium and potassium residues

4) 10 min O_2-Plasma treatment
aim: render the surface of the Si-wafer hydrophilic for homogeneous drop distribution

For the drop deposition: 50 µL are sufficient to cover the full wafer surface when 1x1 cm^2 wafers are used. In most cases a concentration of 0.03$<$ mol L^{-1} in the drop cast solution is sufficient to obtain a homogeneous surface coverage after drying. Note: Control the surface coverage of drop-deposited samples under the microscope. Further, the crystallization pattern can strongly influence the surface roughness and thus the spectral resolution.

Comment: Plasma treatment. Subjecting the Si-Wafer to O_2 Plasma renders the wafer surface hydrophilic, thus allowing the cast droplet to spread over the entire wafer surface and avoids contraction towards the center when drying. This results in a homogeneous film covering the entire wafer surface after drying, as

opposed to a 3-dimensional crystal structure in the center of the wafer which is often observed when the droplet contracts while drying.

Comment: Recycling of Si wafers. There is absolutely no problem in recycling Si wafers. Do it. The production of highly pure silicon wafers is an energy-intensive process. Properly cleaned Si-wafers do not show higher impurities than new ones. In order to reuse a Si wafer that had a previously drop deposited film on it, wash it twice in an ultrasound bath for 15 minutes in the liquid used for the drop deposition of the last film. Subsequently change the glass beaker and proceed with the regular wafer cleaning protocol (see above).

SI3. The influence of differences in de-ionized H_2O purity on the quality of reference spectra

Sodium (Na) and potassium (K) are observed to leach from glass. Thus, even highly pure H_2O purchased e.g. from Sigma Aldrich can show strong Na and K contaminations depending on how long the water was stored in the glass bottle. These contaminations can considerably affect the reference spectra (compare Figures 4.1 and 4.2). Always use freshly purified water. For purification use dedicated equipment (e.g. Milli-Q or Arium Pro). The resistivity should be optimally > 18.2 $M\Omega\,cm$.

SI4. Procedures for preparation of biological samples for ToF-SIMS blockface imaging

When establishing embedding protocols for ToF-SIMS sample preparation, it is advisable to learn from analogue protocols established for electron microscopy (EM). However, in the long term, an adaptation of these protocols will be needed to suit the specific needs of mass spectrometry. Fixation and embedding techniques in EM are designed to preserve the local ultrastructures. The established protocols for the room temperature study of biological specimen by means of EM

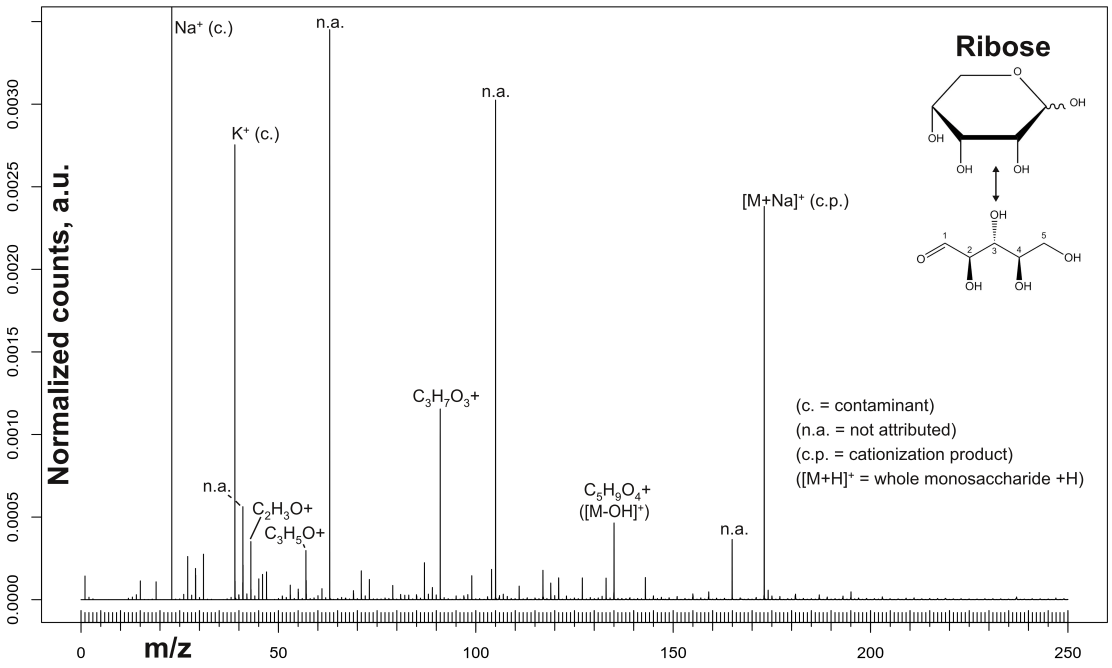

Figure 4.1: Positive polarity ToF-SIMS spectrum of drop-cast D-(-)-Ribose (Sigma Aldrich R7500-5G, Purity: >99 %) as obtained from a 0.1 M solution using deionized water purchased through Sigma Aldrich. The sodium peak has been truncated to visualize the rest of the spectrum. Nearly all larger peaks visible are sodium and potassium cationization products.

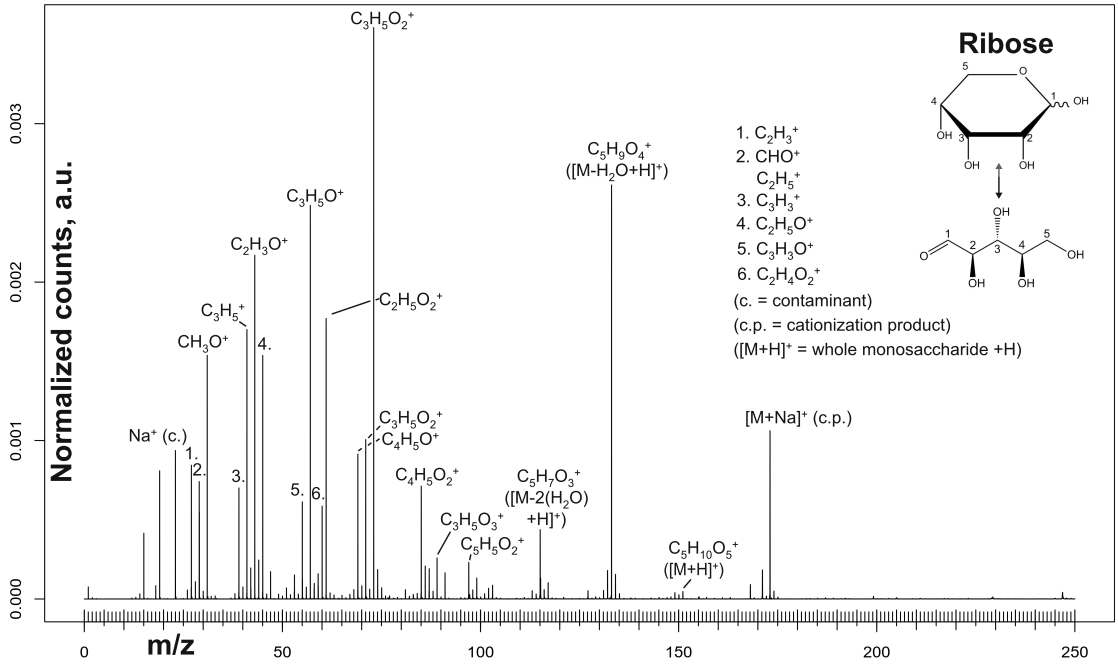

Figure 4.2: Positive polarity ToF-SIMS spectrum of drop-cast D-(-)-Ribose (Sigma Aldrich R7500-5G, Purity: >99 %) as obtained from a 0.1 M solution using freshly deionized water (deionized using Arium Pro UV-B, Resistivity > 18.2 MΩ cm).

rely on chemical crosslinking. For mass spectrometry this is problematic, because crosslinking significantly alters the local chemistry. Nevertheless, whenever elemental analysis is sufficient, or when isotope labeling is an option, preparation methods relying on crosslinking can also be used in SIMS. Preparation methods from fluorescence microscopy require partial preservation of the local chemistry, thus may be better suited for SIMS. Cryofixation and the study of vitrified samples at cryo-temperatures would avoid changes in the local chemistry, however intensive work would be required to allow systematic measurements on vitrified samples using SIMS, as exposure to ambient air has to be avoided throughout the entire sample handling process to avoid ice crystal formation on the surface of the cross section. SIMS is sensitive to the top few molecular layers, thus ice crystal formation is a major obstacle.

While a large variation of preparation protocols can be found in literature, it is observed that the timing and details in their execution are often as important as the individual protocol steps. This is however often omitted in the available literature due to being considered common knowledge. Future students are advised to not shy away from consulting external specialists if preparation outcomes are dissatisfactory despite carefully following the single protocol steps. The most important instances where the execution of a particular protocol step may be decisive for the success of the outcome are highlighted in the report below as in-text notes or numbered comments. Note, preparation steps might be sample-dependent.

Chemical fixation of tissue and unicelluar organisms using aldehydes:

Chemical fixation allows cells and tissue to be preserved throughout the embedding procedures necessary for later sectioning. Most commonly, the aldehydes formaldehyde or glutaraldehyde are used for chemical fixation. Aldehydes crosslink the proteins. It is recommended that tissues not exceed 1 mm thickness in at least one of the dimensions to assure full penetration of the fixing agent. In general, the fixation time strongly depends on temperature, sample dimensions and penetration rates in the sample[112]. In the case of microalgae, which were the main study subject in this project and which shall serve as example throughout the present

report, the fixation was conducted by suspending the cells for 1h15 in MOPS buffer containing 2.5 % glutaraldehyde. After chemical fixation, the sample can be dehydrated and embedded in a resin while preserving its ultrastructure.

Protocol for preparing chemically fixated cell suspensions prior to dehydration and embedding:

Embedding cells or tissue in a resin allows their sectioning at room temperature and so embedded sample material can be conserved for several years. Depending on the sample nature, specific preparation is required prior to embedding in resin. In particular for cell suspensions, the cells first need to be grouped together. Two approaches to locally concentrate the cells are described: clustering and holding in place of the cells in an agar matrix (a), or trapping of the cells in a capillary tube (b).

a) Embedding the cells in agar

a.1) Prepare an agar solution. Stock solutions can be stored in gel-form in a fridge. If the stock solution is used, slowly heat up the stock solution in a microwave by placing the Falcon tube with the agar gel in a water glass in order to avoid overheating.

a.2) Transfer the Falcon tube with the agar in a water bath that is maintained at a controlled temperature between 50 and 60°C. Note, the agar must remain liquid. Put the Eppendorf tubes containing centrifuged down cell pellets in a rack in the water bath such, that the Eppendorf tubes are nearly entirely submerged but without water entering.

a.3) Remove supernatant above the pellets with a pipette.

a.4) Add agar while mixing quickly with the pipette and while keeping as far as possible in the water-bath. After mixing, leave the Eppendorf tube for ca 1-2 min in the water-bath to assure penetration of the agar. Note, the solution must

remain liquid at all times until this point.

a.5) Very quickly transfer the Eppendorf tube out of the water bath and to a centrifuge to form a pellet in the agar. The centrifuging must take place while the agar is still fully liquid.

a.6) Put the Eppendorf tube after centrifuging in ice for several minutes until the agar is fully gelified.

a.7) Take out the Eppendorf tube. With a razor blade cut of the tip of the Eppendorf tube such that the entire pellet is now in the cut of tip.

a.8) With a tiny spatula remove the pellet in one piece from the Eppendorf tip.

a.9) Divide the pellet into small cubes (< 1 mm^3) using a razor blade

a.10) Put the sample cubes in buffer or continue directly with dehydration

b) Embedding cells in capillary tubes

For this approach, capillary tubes intended for medical use in kidney dialysis can be used.

b.1) Centrifuge down the cells in an Eppendorf tube to form a pellet. Remove 4/5 of the liquid and re-suspend the cells to create a more concentrated solution.

b.2) Dip the tip of a ca. 3 cm long capillary tube into the cell suspension. (Tube should/can be dry for this) Note, in the case of microalgae, the tube visibly becomes green as the cells are sucked in and this is visible by naked eye.

(b.3) Directly put the tube in hexadicine in a glass petri dish if cryofixation is intended.)

b.4) Cut the tube in small segments. Using a blunt scalpel - this way the segment ends are sealed. Verify under the microscope that the ends are sealed (You can also see the cells inside the capillary tube with a light microscope)

b.5) Proceed with dehydration.

Protocol for dehydration and embedding of chemically fixated sample material:

Fixated tissue can be directly prepared in small fragments (< 1 mm^3) in order to proceed with dehydration and embedding. The process requires repeated sample transfer between solutions consisting of, in a first step buffer/solvent with increasing fraction of solvent to buffer (dehydration process), and in a second step solvent/Resin with increasing fraction of Resin to solvent (embedding process). IMPORTANT: Never in any of the transfer processes may the sample have the possibility to dry, which would irreversibly destroy the sample - working fast and carefully is crucial!

Dehydration:

1) 20 min 30 % Acetone, 70 % MOPS buffer

2) 20 min 50 % Acetone, 50 % MOPS buffer

3) 20 min 75 % Acetone, 25 % MOPS buffer

5) 20 min 95 % Acetone, 5 % MOPS buffer

6) 10 min 100 % Dehydrated acetone

7) 10 min 100 % Dehydrated acetone

8) 1 h 100 % Dehydrated acetone

Embedding:

8) 5 h at 4°C in 33 % Epon prepared with only 50 % of accelerator (DMP30) in the mixture and 66 % dehydrated acetone.

9) 15 h at 4°C in 66 % Epon prepared with only 50 % of accelerator (DMP30) in the mixture and 33 % dehydrated acetone.

10) 5 h at 4°C in 90 % Epon prepared with only 50 % of accelerator (DMP30) in the mixture and 10 % dehydrated acetone.

11) 1 h at 4°C in 100 % Epon prepared with 90 % of accelerator (DMP30) in the mixture

12) Fill designated silicon forms with the Epon and position one sample per form as much as possible at the tip. Note, the Epon is highly viscous, be vary careful to not include any air bubbles!

13) Transfer the forms into the oven and let harden at 60°C over 24 hours.

Protocol for cryo-fixation of unicellular organisms by high pressure freezing:

The protocol is exemplified on the preparation of suspended cell media.

1) Centrifuge cells in Eppendorf tubes to form a cell pellet at the bottom of the tube (1800 rpm, 10 min)

2) Remove supernatant with a pipette.

3) Transfer cell pellet using spatula to the 100 μm cavity of a 3 mm gold coated copper specimen carrier.

4) close the carrier with a flat 3 mm gold coated copper specimen carrier wetted with 1-hexadecene.

5) Transfer carrier into the ICE HPF. Remaining procedure automatized. The cryo-fixated samples are dropped into liquid nitrogen from where they can either be studied as such or further processed by freeze-substitution.

Protocol for freeze-substitution and embedding of cryo-fixated sample material:

If a cryo-fixated specimen cannot be studied at cryo-temperatures, freeze-substitution and subsequent embedding can be employed. Freeze-substitution and embedding of cryo-fixated sample material require, much like high-pressure freezing itself, specialized equipment (e.g. the **Leica EM AFS2 automatic freeze substitution system**). The general idea of freeze substitution is to gradually dehydrate the sample by replacing water molecules in the frozen sample by solvent molecules. This is achieved by submerging the frozen sample in pure solvent at very low temperature and gradually ramping up the solvent temperature over a duration of 1-7 days until ambient temperature is reached. The replacement of water molecules is the first step in a two-step process, the second being a subsequent gradual replacement of the solvent by a resin allowing the sample to be solidified. Cryo-fixation -> Freeze substitution -> Resin embedding has a two advantages over Chemical fixation -> Resin embedding:

a) The ultrastructure is better preserved and less deformation occurs in the cells.

b) Freeze-substitution allows aldehyde fixation to be bypassed.

Later, in the resin embedding following freeze-substitution crosslinking with molecules of sample origin can be minimized if acrylic resin is used which mainly crosslinks with itself.

The freeze substitution steps may need to be adapted depending on sample material and size[113]. The protocol used to embed the microalgal samples is the following:

1) Immerse the samples (still in their Al-plates from high-pressure freezing) into anhydrous acetone containing 1 % osmium tetroxide cooled to -90°C and contained in separate Eppendorf tubes in the cooled apparatus for freeze-substitution. (Note, the osmium tetroxide crosslinks membrane lipids, providing a good contrast not only for EM, but also for ToF-SIMS measurements where the osmium peak can be used as aid in finding cell contours)

2) 8h at -90°C

3) 1h linear ramping from -90°C to -60°C

4) 6h at -60°C

5) 1h linear ramping from - 60°C to -30°C

6) 4h at -30°C

7) 1h linear ramping from -30° to 0°C

8) 4h at 0°C

9) Open Eppendorf tubes for pressure equilibration. **!NOTE! :** When doing this, safety glasses are needed as during the temperature increase process the pressure build-up through evaporation can be sufficient to allow for eye contamination with osmium tetroxide-containing droplets upon tube opening. Also, open tube towards the direction away from yourself.

10) Transfer Eppendorf tubes into a rack and leave for 1h at room temperature.

11) (If osmium was used) Wash the samples x2 in Eppendorf tubes with pure anhydrous acetone.

12) Remove Al plates

13) Proceed with embedding in resin by gradually increasing the resin content in the solvent (see previous sections).

Comment 1: Transfer of vitrified samples into the ToF-SIMS instrument. Chemical fixation and resin embedding leads to significant changes in the local chemistry which, while irrelevant for EM, is detrimental in ToF-SIMS. As ToF-SIMS instruments can be equipped with a cold finger allowing a sample temperature of 100-150 K to be maintained within the instrument, it is conceivable to fully avoid chemical fixation and embedding by directly studying untreated, high pressure frozen samples. For this, however, solutions have to be found first to avoid rapid ice crystal formation on the sample surface during transfer, as ToF-SIMS measures the top few molecular layers and a layer of atmospheric H_2O will render measurements impossible. There are two considerations that could provide a first step towards tackling the problem:

a) line-of-sight shielding by a previously liquid nitrogen cooled metallic shield trapping incoming water molecules is known to efficiently prevent ice crystal formation on the sample surface. Note, the shield potentially does not need to be hermetic and the trajectories of most water molecules can be approximated as straight lines through space at the relevant length scales. Line-of-sight shielding of the sample surface is observed to be sufficient for the purposes of SEM, thus it might be sufficient for ToF-SIMS as well.

b) The transfer can be made in a N_2-flushed 'glove box', made from plastic foil. Such a construction is already available in the Empa ToF-SIMS lab, but has not been tested yet by the author of this report.

An attempt can be made to sublimate the ice by keeping the sample at cryo-

temperature and UHV inside the instrument for a sufficient amount of time. This praxis is employed in cryo-EM[114].

Comment 2: Embedding and crosslinking. Alternatively to measuring vitrified samples maintained at cryo-temperature, dedicated embedding techniques exist to minimize crosslinking. In particular dedicated sample preparation protocols for the overlay of both EM and fluorescence microscopy images cannot afford pronounced cross-linking[115,116]. These dedicated protocols often make use of acrylic resins (e.g. HM20[117]) which crosslink mainly with itself, which may prove highly useful for sufficient preservation of the local chemistry for the ToF-SIMS study of resin-embedded specimens.

Comment 3: Charging behavior of the embedding medium. For the potential future 3D-imaging of resin-embedded specimen by in-situ microtomy, a major challenge will be that the sample surface must be comparatively small and with strongly dropping edges to allow sectioning, while the sample material itself is highly nonconductive. These sample properties can be expected to lead to pronounced secondary ion signal loss due to charging effects.

Charging effects are also problematic in EM blockface imaging and the solutions developed there might be adopted. Among the approaches to render the resin more conductive is the inclusion of carbon black[118] or carbon nano-fibres[119] in the resins used.

In EM blockface imaging, Durcopan is sometimes used as resin instead of Epon, as less charging is observed[120]. These protocols were not tested for ToF-SIMS, but may provide an alternative for tackling charging-induced secondary ion signal loss.

Acknowledgements

Funding for these studies was provided by the Swiss National Science Foundation (SNF) (grant number CR23I2-162828) and Empa, the Swiss Federal Laboratories for Materials Science and Technology. Dr. Laetitia Bernard was the PI of the project together with Prof. Dr. J. G. Snedeker and Prof. Dr. H. J. Hug as co-PIs. The Thesis was jointly supervised by Dr. Rowena Crockett, Dr. Laetitia Bernard and Prof. Dr. Hans Josef Hug (no particular order intended). Quantum chemistry calculations were conducted by Dr. Daniele Passerone at Empa Dübendorf, at the Nanotech@Surfaces Laboratory. The author also wishes to thank:

The engineer Saša Vranjkovic at the Laboratory for Nanoscale Materials Science for his assistance in the design of two in-situ microtomes for ToF-SIMS.

The engineers at the workshop of Empa Dübendorf for the manufacturing of the microtome components.

The engineer Günther Hobi at the Laboratory for Nanoscale Materials Science for the design and assembly of custom electrical components.

Dr. Ulrich Müller at the Laboratory for Nanoscale Materials Science for providing access to the Bruker atomic force microscope.

Dr. Jakob Heier at the Laboratory for Functional Polymers for providing access to the profilometer.

Matthias Diethelm, Sandra Jenatsch and Roland Steim at the Laboratory for Functional Polymers for transferring their knowledge on the fabrication of LECs.

Dr. Roland Hany at the Laboratory for Functional Polymers for providing access to his laboratories and equipment, and for taking the role of an unofficial additional supervisor in a large part of this project.

Prof. Dr. Jess G. Snedeker at the University Hospital Balgrist for numerous fruitful discussions and general support.

Dr. Stephanie Merbt, Bettina Wagner and Prof. Dr. Renata Behra at the Department for Environmental Toxicology at Eawag for a highly instructive long-term collaboration that regrettably did not fruit in a publication.

Dr. Andres Käch, Ursula Lüthi and Carmen Kaiser at the Center for Microscopy and Image Analysis at the University of Zürich for deep insight into sample preparation methods for electron microscopy, numerous fruitful discussions, support, and the permission to use their instrumentation.

The multitude of Scientists that contributed to this project by sharing their ideas and knowledge in discussions and by personal e-mail exchange, but are not listed here by name.

Curriculum Vitae

Name: Maciej Kawecki-Wenger
Date of Birth: 22.09.1990
Nationality: Polish

Education:

2016-2019: Doctoral studies in **Physics** (*University of Basel, Basel, Switzerland*)
2013-2015: Master of Science in **Physics** (*Uppsala Universitet, Uppsala, Sweden*)
2010-2013: Bachelor of Science in **Physics** (*Universität Fribourg, Fribourg Switzerland*)
2006-2010: Eidgenössische Matura (*Collège St. Michael, Fribourg, Switzerland*)

Publication list

[1] M. Kawecki*, R.Hany, M.Diethelm, S.Jenatsch, Q.Grossmann, L.Bernard* and H.J. Hug; *Direct measurement of ion redistribution and resulting modification of chemical equilibria in polymer thin film light-emitting electrochemical cells*; ACS Appl. Mater. Interf. **10**, 39100 (2018)

[2] S. Bai*, P. Da, C. Li, Z. Wang, Z. Yuan, F. Fu, M. Kawecki, X. Liu, N. Sakai, J.T.-W. Wang, S. Huettner, S. Buecheler, M. Fahlman, F. Gao* and H.J. Snaith*; *Planar perovskite solar cells with long-term stability using ionic liquid additives*; Nature **571**, 245-250 (2019)

[3] W. Xu, Q. Hu, S. Bai, C. Bao, Y. Miao, Z. Yuan, T. Borzda, A.J. Barker, E. Tyukalova, Z. Hu, M. Kawecki, H. Wang, Z. Yan, X. Liu, X. Shi, K. Uvdal, M. Fahlman, W. Zhang, M. Duchamp, J.-M. Liu, A. Petrozza, J. Wang, L.-M. Liu*, W. Huang* and F. Gao*; *Rational molecular passivation for high-performance perovskite light-emitting diodes*; Nature Photonics **13**, 418-424 (2019)

[4] F. Fu*, S. Pisoni, Q. Jeangros, J. Sastre-Pellicer, M. Kawecki, A. Paracchino, T. Moser, J. Werner, C. Andres, L. Duchene, P. Fiala, M. Rawlence, S. Nicolay, C. Ballif, A. N. Tiwari and S. Buecheler; *I2 vapor-induced degradation of formamidinium lead iodide based perovskite solar cells under heat-light soaking conditions*; Energy and Environmental Science **12**, 3074-3088 (2019)

[5] M. Diethelm, Q. Grossmann, A. Schiller, E. Knapp, S. Jenatsch, M. Kawecki, F. Nuesch and R. Hany*; *Optimized electrolyte loading and active film thickness for sandwich polymer light-emitting electrochemical cells*; Adv. Opt. Mater., 1801278 (2019)

[6] M. Diethelm, A. Schiller, M. Kawecki, A. Devizis, B. Blülle, S. Jenatsch, E. Knapp, Q. Grossmann, B. Ruhstaller, F. Nüesch and R. Hany*; *The dynamic emission zone in sandwich polymer light-emitting electrochemical cells*; Adv. Funct. Mater., 1906803 (2019)

[7] M. J. I. Airaghi Leccardi, N. A. L. Chenais, L. Ferlauto, M. Kawecki, E. G. Zolliger, and D. Ghezzi*. *Tailored polymeric, photovoltaic, and near-infraredresponsive neuroprosthesis.* Nature Communications, in review

[8] M. Kawecki* and L. Bernard; *Database of proteinogenic amino acid reference spectra for bismuth-cluster ToF-SIMS. I. Negative polarity*; Surf. Sci. Spectra **25**(1), 015001 (2018)

[9] M. Kawecki* and L. Bernard; *Database of proteinogenic amino acid reference spectra for bismuth-cluster ToF-SIMS. II. Positive polarity*; Surf. Sci. Spectra

25(1), 015002 (2018)

[10] L. Bernard, R. Crockett and M. Kawecki*, *Monosaccharides: a ToF-SIMS reference spectra database. I. Negative polarity*; Surf. Sci. Spectra **26**(2), 025001 (2019)

[11] L. Bernard, R. Crockett and M. Kawecki*, *Monosaccharides: a ToF-SIMS reference spectra database. II. Positive polarity*; Surf. Sci. Spectra **26**(2), 025002 (2019)

[12] M. Kawecki*, L. Bernard, D.Passerone, H.J. Hug and R. Crockett; *Supramolecular secondary ions reveal molecular interactions in organic matter*; submitted

[13] A. Mairena M. Baljozovic, M. Kawecki, K. Grenader, M. Wienke, K. Martin, L. Bernard, N. Avarvari, A. Terfort, K.-H. Ernst* and C. Wäckerlin*; *The fate of bromine after temperature-induced dehydrogenation of on-surface synthesized bisheptahelicene*; Chemical Science **10**, 2998 (2019)

[14] T. Razafiarison C.N. Holenstein, T. Stauber, M. Jovic, E. Vertudes, M. Loparic, M. Kawecki, L. Bernard, U. Silvan and J.G. Snedeker*; *Biomaterial surface energy-driven ligand assembly strongly regulates stem cell mechanosensitivity and fate on very soft substrates*; PNAS **115**, 4631 (2018)

[15] M. Kawecki*, *Bitcoin mining built on shifting sands*; Nature **557**, 166 (2018)

[16] M. Kawecki, F. A. Adlmann, P. Gutfreund, P. Falus, D. Uhrig, S. Gupta, B. Farago, P. Zolnierczuk, M. Cohran and M. Wolff*; *Direct measurement of topological interactions in polymers under shear using Neutron Spin Echo spectroscopy*; Sci. Rep. **9**, 2823 (2019)

[17] A. Korokovas*, S. Prevost, M. Kawecki, A. Devishvili, F. A. Adlmann, P. Gutfreund and M. Wolff; *The viscoelastic signature underpinning polymer deformation under shear flow*; Soft Matter **15**, 371-380 (2019)

[18] F. A. Adlmann*, G. K. Palsson, J. C. Bilheux , J. F. Ankner, P. Gutfreund, M. Kawecki and M. Wolff; *Överlataren: a fast way to transfer and orthogonalize two-dimensional off-specular reflectivity data*; J. Appl. Cryst. **49**, 2091-2099 (2016)

[19] M. Kawecki*, P. Gutfreund, F. A. Adlmann, E. Lindholm, S. Longeville, A. Lapp and M. Wolff*; *Probing the dynamics of high-viscosity entangled polymers under shear using Neutron Spin Echo spectroscopy*; J. Phys. Conf. Ser. **746**, 012014 (2016)

* corresponding author